The Alzheimer's disease risk gene *BIN1* modulates neural network activity via the regulation of L-type calcium channel expression in human-induced neurons

Orthis Saha[1,#], Ana Raquel Melo de Farias[1,2,#], Alexandre Pelletier[3,#,&], Dolores Siedlecki-Wullich[1], Johanna Gadaut[1], Bruna Soares Landeira[1], Arnaud Carrier[3], Anaïs-Camille Vreulx[1], Karine Guyot[1], Amelie Bonnefond[3], Philippe Amouyel[1], Cláudio Marcos Queiroz[2], Devrim Kilinc[1], Fabien Delahaye[3], Jean-Charles Lambert[1] and Marcos R. Costa[1,2,*]

1. Univ. Lille, Inserm, CHU Lille, Institut Pasteur de Lille, U1167-RID-AGE facteurs de risque et déterminants moléculaires des maladies liées au vieillissement, DISTALZ, Lille, France
2. Brain Institute, Federal University of Rio Grande do Norte, Natal, Brazil
3. Univ. Lille, Inserm, CNRS, CHU Lille, Institut Pasteur de Lille, U1283-UMR 8199 EGID, Lille, France

[#]Equal contribution

[&]Current address: The Department of Pharmacology, Physiology & Biophysics. Boston University, Chobanian & Avedisian School of Medicine, MA 02118

* Correspondence should be addressed to:

Marcos Costa, MD, PhD
INSERM UMR1167
Institut Pasteur de Lille
1 rue du Pr. Calmette
59019 Lille CEDEX, France
Tel: 00 33 (0)3 20 87 77 10
marcos.costa@pasteur-lille.fr

Keywords : Human induced neurons ; cerebral organoids ; BIN1 ; neuronal electrical activity ; gene expression ; Alzheimer's disease ; calcium homeostasis

Abstract

Background: Bridging Integrator 1 (*BIN1*) is the second most important Alzheimer's disease (AD) risk gene, but its physiological roles in neurons and its contribution to brain pathology remain largely elusive. In this work, we show that BIN1 plays a critical role in the regulation of calcium homeostasis, electrical activity, and gene expression of glutamatergic neurons.

Methods: We generated 3D cerebral organoids and 2D enriched neuronal cell cultures from isogenic *BIN1* wild-type (WT), heterozygous (HET) and homozygous knockout (KO) human-induced pluripotent stem cells (hiPSCs). Using single-cell RNA-sequencing, biochemical assays, immunocytochemistry and multi-electrode array(MEA) electrophysiology, we characterized the molecular and functional consequences of reduced BIN1 expression in different neural cell types.

Results: We show that *BIN1* is mainly expressed by oligodendrocytes and glutamatergic neurons of cerebral organoids, like in the human brain. Both *BIN1* HET and KO cerebral organoids show specific transcriptional alterations, mainly associated with ion transport and synapses in glutamatergic neurons. We then demonstrate that *BIN1* cell-autonomously regulates gene expression in glutamatergic neurons by using a novel protocol to generate pure culture of human-derived induced neurons (hiNs). Using this system, we also show that BIN1 plays a key role in the regulation of neuronal calcium transients and electrical activity via its interaction with the L-type voltage-gated calcium channel $Cav_{1.2}$. *BIN1* KO hiNs show reduced activity-dependent internalization and higher $Cav_{1.2}$ expression compared to WT hiNs. Pharmacological treatment with clinically relevant doses of nifedipine, a calcium channel blocker, partly rescues neuronal electrical and gene expression alterations in *BIN1* KO glutamatergic neurons. Further, we show that transcriptional alterations in *BIN1* KO hiNs affecting biological processes related to calcium homeostasis are also present in glutamatergic neurons of the human brain at late stages of AD pathology.

Conclusions: Together, our findings suggest that BIN1-dependent alterations in neuronal properties could contribute to AD pathophysiology and that treatment with low doses of clinically approved calcium blockers should be considered as an option to dampen disease onset and progression.

61 ## Introduction

62 The Bridging Integrator 1 (*BIN1*) is the second most associated genetic determinant
63 with the risk of late-onset Alzheimer's disease (LOAD), after the Apolipoprotein E (*APOE*)
64 gene [1–4]. In the adult human brain, *BIN1* is mainly expressed by oligodendrocytes,
65 microglial cells and glutamatergic neurons [5–7] and its expression is reduced in AD patients
66 compared to healthy individuals [7,8]. The consequences of this reduced BIN1 expression to
67 neuronal and glial cells, as well as the mechanisms by which it contributes to AD
68 pathogenesis remain poorly understood.

69 BIN1 has disputably been associated with amyloidopathy and tauopathy, two
70 pathological hallmarks of AD [9]. Reduced BIN1 expression results in a higher amyloid
71 precursor protein (APP) processing towards the production of amyloid-beta (Aβ) peptides in
72 Neuroblastoma Neuro2a cells [10,11]. However, we previously showed that *BIN1* knockout
73 (KO) does not increase the concentrations of Aβ peptides in hiPSC-derived neurons (human-
74 induced neurons or hiNs) despite impairing endocytic trafficking [12]. Likewise, reduced
75 Bin1 expression in the mouse brain does not affect the production of endogenous Aβ
76 peptides [13]. Concerning Tau pathology, decreased expression of the BIN1 ortholog Amph
77 suppress Tau-mediated neurotoxicity in Drosophila Melanogaster [14]. In contrast, reduced
78 BIN1 expression results in higher Tau aggregation and propagation in primary rat
79 hippocampal neurons [15]. In humans, higher concentrations of phosphorylated Tau are
80 observed in the cerebrospinal fluid of patients with AD and are significantly correlated with
81 genetic variants within the *BIN1* locus [16].

82 More recently, BIN1 has also been associated with the regulation of synaptic
83 transmission and neuronal electrical activity in animal models. Conditional deletion of *Bin1*
84 in neurons of the adult mice hippocampus leads to altered frequency of mini excitatory
85 post-synaptic currents (mEPSC), likely due to an impaired presynaptic release probability
86 and slower depletion of neurotransmitters [6]. Knockdown of *BIN1* in embryonic rat primary
87 cortical neurons also affects the glutamate AMPA receptor trafficking in the post-synaptic
88 compartment, leading to alterations in the amplitude of mEPSC [17]. Lastly, overexpression
89 of a BIN1-mKate2 fusion protein increases the frequency of spontaneous excitatory
90 postsynaptic currents (sEPSCs) in embryonic rat hippocampal cultures, seemingly by

91 affecting the localization of L-type voltage gated calcium channels (LVGCC) in the membrane
92 through a Tau-dependent interaction [18].

93 Despite these advances, no consensus has been reached on the roles of BIN1 in AD
94 pathogenesis and even its physiological functions in human brain cells remain mostly
95 unknown. In this work, we tackled this important question by generating and characterizing
96 human neural cells derived from isogenic *BIN1* wild type (WT), heterozygous (HET) and
97 homozygous knockout (KO) hiPSC lines. We first characterized the transcriptional profile of
98 human neural cells grown in three-dimensional cerebral organoids for more than 6 months
99 and show that reduced BIN1 expression affects mainly glutamatergic neurons. Next, we
100 generated pure *BIN1* WT and KO hiNs cultures and show that BIN1 cell-autonomously
101 regulates electrical activity and gene expression of glutamatergic neurons via the interaction
102 with the regulation of the LVGCC $Cav_{1.2}$. Pharmacological blockage of this channel with
103 nifedipine partly rescues electrical and gene expression alterations in *BIN1* KO hiNs. Our
104 findings suggest that BIN1 is a key regulator of calcium homeostasis in glutamatergic
105 neurons and that repurposing the use of clinically approved calcium channel blockers could
106 be a promising strategy to treat AD.

Results

BIN1 HET and KO cerebral organoids show transcriptional alterations associated with neuronal functional properties

Cerebral organoids (COs) faithfully recapitulate fundamental aspects of the three-dimensional organization of the human brain, including the molecular specification of different neural cell types/subtypes and the generation of complex electrical activity patterns [19,20]. To investigate the potential role of BIN1 in human neural cells, we generated and characterized COs using isogenic *BIN1* wild type (WT), heterozygous (HET) and KO hiPSCs (Fig. 1A). After 6.5 months of culture, COs were composed of all the major neural cell types identified by the expression of MAP2, GFAP and NESTIN and we did not observe any gross difference in size or morphology of COs among the three genotypes (Sup. Fig. 1A). Western blot analyses confirmed the reduction and absence of BIN1 protein in BIN1 HET and KO COs, respectively (Sup. Fig. 1B). We have then employed single-nucleus RNA sequencing (snRNA-seq) to further characterize individual cell types/subtypes and investigate possible gene expression alterations associated with reduced BIN1 expression. COs (n=4 from each genotype) were divided into two halves that were independently processed for western blotting or snRNA-seq. We observed similar expression of general neuronal and glial proteins in these COs (Sup. Fig. 1C), suggesting a low degree of heterogeneity in these samples. Nevertheless, to further reduce potential batch effects, we pooled COs into a single multiplexed library using Cell Hashing (Stoeckius et al., 2018). After sequencing, quality control and demultiplexing, we recovered 4398 singlets that could be grouped into 7 major cell clusters based on the expression of cell type markers *SLC1A3 (GLAST), GFAP* and *TNC* (astrocyte); *SNAP25, DCX, MAPT* (pan-neuronal); *SLC17A7* and *SLC17A6* (glutamatergic neurons); *DLX1, GAD1* and *GAD2* (GABAergic neurons); *HES6, CCND2* and *CDK6* (NPCs); *ITGA8* (choroid plexus); and *CLIC6* (pigmented epithelium) (Fig. 1B-C). *BIN1* expression in COs was mainly detected in glutamatergic neurons and oligodendrocytes (Fig. 1C), similar to the profile described for the human brain [7] - except for brain microglial cells that express *BIN1* but are not present in COs. We also observed a reduction and enlargement, respectively, in the proportions of glutamatergic neurons and astrocytes in *BIN1* KO compared to WT (Fig. 1D; ****$p<0.0001$; Chi-square test).

138 To identify possible differentially expressed genes (DEGs) in *BIN1* KO or HET compared
139 to WT cells, we performed Wilcoxon test for each major cell type/subtype identified in COs.
140 Consistent with the predominant expression of *BIN1* in glutamatergic neurons (Fig. 1D), we
141 identified a high number of DEGs in this cell type both in *BIN1* HET (76 genes) and KO (124
142 genes) compared to WT genotype (Fig. 1E; Sup. Fig. 1D). In astrocytes, we also detected 75
143 DEGs in *BIN1* KO, but only 6 DEGs in *BIN1* HET compared to WT (Fig. 1E; Sup. Fig. 1D). For all
144 other cell types, we observed a maximum of 1-4 DEGs in the comparison between KO vs WT
145 or HET vs WT (Sup. Table 1). These observations suggest that both BIN1 null (KO) and partial
146 deletion (HET) affect similar biological process in glutamatergic neurons in a dose-
147 dependent manner. Accordingly, similar GO terms were enriched for DEGs identified in *BIN1*
148 KO or HET glutamatergic neurons, including several terms associated with synaptic
149 transmission (Fig. 1F). For *BIN1* KO glutamatergic neurons, we also identified GO terms
150 associated with ion channel complex and calcium ion binding (Sup. Fig. 1E; Sup. Table 2),
151 further suggesting that BIN1 depletion leads to specific transcriptional changes associated
152 with functional properties of this neuronal subtype.
153
154 **Altered expression of activity-related genes in *BIN1* KO and HET COs**
155 Neuronal firing patterns (such as tonic and burst firing) play a key role on the
156 transcriptional regulation of a particular set of genes designated activity-related genes
157 (ARGs) [21]. While neurons stimulated with brief patterns of electrical activity transcribe
158 rapid primary response genes (rPRGs) or early response genes (ERGs), those stimulated with
159 sustained patterns of electrical activity express delayed primary response genes (dPRGs),
160 secondary response genes (SRGs) or late response genes (LRGs) (Fig. 2A)[22,23]. Using Cell-
161 ID [24], we quantified the enrichment for ARGs signatures (Sup. Table 3) in COs at single-cell
162 resolution as an indirect read-out of neuronal electrical activity patterns in this model. We
163 first confirmed that ARG signatures were predominantly enriched in neurons (Fig. 2B).
164 Then, we quantified the proportion of glutamatergic or GABAergic neurons significantly
165 enriched for such specific response gene signatures ($p_{adj}<0.05$; hypergeometric test). We
166 observed a significantly higher proportion of glutamatergic neurons enriched for dPRGs and
167 LRGs both in *BIN1* HET and KO, as well as SRGs in *BIN1* KO compared to WT glutamatergic
168 neurons, whereas the proportion of glutamatergic neurons enriched for rPRGs and ERGs
169 was reduced in *BIN1* HET and KO (Fig. 2C). In sharp contrast, the only difference observed in

170 GABAergic neurons was a reduction in the proportion of cells enriched for SRGs (Sup. Fig. 2).
171 These results suggest that reduced BIN1 expression in glutamatergic neurons triggers
172 neuronal firing patterns towards sustained activity leading to a higher expression of late-
173 response ARGs.
174
175 **Lower numbers of synaptic *puncta* in BIN1 HET and KO COs compared to WT**
176 Transcriptional alterations in *BIN1* HET and KO glutamatergic neurons are also
177 suggestive of synaptic dysfunction, which is an early hallmark of AD pathology [25]. We thus
178 sought to determine whether BIN1 depletion could affect synaptic connectivity in COs.
179 Using immunohistochemistry to detect the expression of the pre-synaptic protein
180 Synaptohysin-1 (SYP) and post-synaptic protein HOMER1, we were able to quantify the
181 frequency of putative synaptic contacts (% SYP assigned) in COs (see methods). We
182 observed a significant reduction in the % of SYP assigned both in *BIN1* HET and KO
183 compared to WT, mainly due to a reduction in the number of post-synaptic spots expressing
184 HOMER1 (Fig. 3A-D).
185 Next, we investigated whether APP processing and Tau phosphorylation, which have
186 been previously associated with BIN1 and are known to modulate neuronal electrical
187 activity [10,15,26], could also be altered in *BIN1* HET and KO COs. To this end, we measured
188 the intracellular levels of full-length APP and APP β-CTF (as a readout of amyloidogenic APP
189 processing), total and phosphorylated TAU proteins by western blotting. Besides a trend for
190 reduced TAU expression (Fig. 3F) likely explained by the reduced proportion of neurons, we
191 did not detect any significant differences in the intracellular levels of APP, APP β-CTF, TAU or
192 phospho-TAU (Ser202, Thr205) in *BIN1* HET and KO compared to WT COs (Fig. 3E-L).
193 Altogether, these results suggest that BIN1 depletion could alter neuronal functional
194 properties without significantly affecting APP or Tau metabolism in COs.
195
196 **Cell-autonomous role of BIN1 in the regulation of neuronal gene expression**
197 Our results in COs suggest that reduced BIN1 expression affects mainly glutamatergic
198 neurons. However, at least in BIN1 KO COs, we cannot completely rule out an effect of BIN1
199 deletion in astrocytes that could indirectly impact glutamatergic neurons. Therefore, to
200 unambiguously probe the cell-autonomous effect of *BIN1* deletion on the electrical activity
201 and gene expression of human glutamatergic neurons, we generated *BIN1* WT or KO pure

202 neuronal cultures by direct lineage-reprogramming of human NPCs (hNPCs) using
203 doxycycline-inducible expression of ASCL1 (Fig. 4A; see online methods). After validation of
204 the efficient lineage-reprogramming of hNPCs into highly pure neurons (hereafter ASCL1-
205 hiNs) (Fig. 4B), we added exogenous human cerebral cortex astrocytes to trophically support
206 functional neuronal maturation and synaptic connectivity [27]. Using snRNA-seq after 4
207 weeks of differentiation we identified 5583 cells (n=5 independent culture batches)
208 clustered into two main glutamatergic neuron (GluNeu-I and II), one GABAergic neuron
209 (GABANeu), one immature/unspecified neuron (UnspNeu), two astrocyte (Astro-I and II) and
210 1 proliferative NPC groups (Fig. 4C-D). Sample-level differential gene expression analysis
211 using DESeq2 [28], revealed 99 DEGs (|log2FC| >0.25 and FDR <0.05) in *BIN1* KO GluNeu-II
212 compared to WT, but only 2 in GluNeu-I and 1 in immature neurons (Fig. 4E; Sup. Table 4).
213 As observed in COs (Fig. 1H-I), GO term enrichment analysis revealed a significant
214 enrichment for terms associated with synaptic transmission, ion channel activity and
215 calcium signaling pathways (Fig. 4F; Sup. Table 5). The percentage of GluNeu-II enriched for
216 late-response ARGs was slightly greater in *BIN1* KO compared to WT, but without statistical
217 differences (Fig. 4G-H). Exogenously added human astrocytes co-cultured with *BIN1* WT and
218 KO hiNs also showed a low number of DEGs (11 in Astro-I; Sup. Table 4), likely reflecting an
219 astrocyte reaction to primary changes in hiNs in response to *BIN1* deletion.
220
221 ***BIN1* KO leads to alteration in the electrical activity pattern of ASCL1-hiNs**
222 The transcriptional changes observed in our 2D and 3D models could suggest that
223 reduced BIN1 expression is associated with altered electrical properties of glutamatergic
224 neurons. To directly address this possibility, we used multi-electrode arrays (MEA) to record
225 and quantify multi-unit activity (MUA) in ASCL1-hiNs. As previously described in
226 spontaneously differentiated hiPSC-derived neuronal cultures [29], ASCL1-hiNs cells
227 exhibited a diverse range of spontaneous activity patterns, including regular discharges,
228 population bursts and period activity (Fig. 5A). In this respect, we found a conspicuous
229 change in the temporal organization of MUA after *BIN1* deletion (Fig. 5A), mainly
230 characterized by a greater number of spike bursts at 4 weeks (Fig. 5D). These alterations
231 may result from changes at the single cell or the population level (different number of
232 neurons contributing to each electrode, for example). To disentangle these possibilities, we
233 used waveform-based spike sorting to examine the functional consequences of *BIN1*

234 deletion at the single neuronal level (Fig. 6A). We identified a similar number of single units
235 per recording electrode between genotypes (WT: 4.92±2.34; KO: 5.27±2.45), indicating that
236 *BIN1* deletion does not affect the density of active neurons within culture. However, we
237 observed reduced single-unit activity (SUA) frequency (Fig. 6B) and higher SUA amplitude
238 (Fig. 6C) in *BIN1* KO compared to WT ASCL1-hiNs. Interestingly, we could not detect
239 significant changes in the number of bursts per neuron (WT: 11.01±6.71; KO: 10.36±8.59),
240 although both the burst duration and the number of spikes within a burst were significantly
241 lower in *BIN1* KO compared to WT ASCL1-hiNs (Fig. 6D-E). We also observed a prominent
242 temporal disorganization of *BIN1* KO hiNs activity by computing the array-wide spike
243 detection rate (ASDR, Fig. 6G), which reveals the strength of the synchronized population
244 activity, and the autocorrelograms of SUAs (Fig. 6H-I), which allows the apprehension of
245 synchronized periodicity. These analyses revealed that most spikes of *BIN1* WT neurons
246 were organized in bursts occurring at periodic intervals of about 8-10 s, whereas the spikes
247 of *BIN1* KO neurons were randomly distributed, leading to a higher percentage of spikes
248 occurring outside of bursts compared to WT neurons (Fig. 6J).
249
250 **Altered electrical activity of *BIN1* KO ASCL1-hiNs is associated with normal synapse**
251 **numbers and altered TAU phosphorylation**
252 These changes in neural network activity observed in *BIN1* KO hiNs could be explained,
253 among other things, by a reduced synaptic connectivity, as observed in our long-term COs
254 cultures (Fig. 3). To test this possibility, we first quantified the number of synaptic contacts
255 in *BIN1* WT and KO ASCL1-hiNs cultures. In contrast with COs, we did not detect any
256 significant differences in the number of putative synaptic contacts (% SYP assigned) in *BIN1*
257 KO compared to WT ASCL1-hiNs, neither after 4 nor 6 weeks of differentiation (Fig. 7A-D).
258 Next, we quantified the number and activity of glutamatergic synapses by using real-time
259 imaging of ASCL1-hiNs expressing the glutamate sensor iGLUSnFr [30]. In accordance with
260 our observations based on immunocytochemistry, we did not detect differences neither in
261 the number of glutamatergic synapses (active spots) nor in the frequency of events (change
262 in fluorescence levels in active spots) in *BIN1* KO compared to WT ASCL1-hiNs (Sup. Fig. 3;
263 Sup. Movies 1 and 2), indicating that changes in neuronal activity observed in our cultures
264 are not related to changes in synaptic transmission.

265 Taking advantage of this culture system comprising enriched neuronal populations, we
266 also sought to confirm whether BIN1 deletion could be associated with changes in APP
267 processing or Tau phosphorylation. To this end, we measured the extracellular levels of
268 amyloid-beta (Aβ) peptides, as well as the intracellular levels of full-length APP and APP β-
269 CTF, total and phosphorylated TAU proteins in ASCL1-hiNs cultures. Like COs, we did not
270 detect any significant differences neither in the extracellular levels of Aβ1-x or Aβ1-42, nor
271 in the intracellular levels of APP or APP β-CTF in *BIN1* KO compared to WT ASCL1-hiNs (Sup.
272 Fig. 4). However, in contrast with our observations in COs, we observed significantly higher
273 levels of phospho-TAU (Ser202, Thr205) relative to β-ACTIN and total TAU in in *BIN1* KO
274 compared to WT ASCL1-hiNs (Fig. 7E-F). Together, these observations may suggest that *BIN1*
275 deletion primarily impairs neuronal intrinsic properties regulating electrical activity and Tau
276 phosphorylation prior to detectable changes in synaptic communication (observed only in
277 long-term cultures) and independently of alterations in APP processing.
278
279 **BIN1 regulates neuronal Ca^{2+} dynamics through LVGCCs**
280 In neurons, electrical activity is always accompanied by an influx of Ca2+ ions, which
281 play a fundamental role in the regulation of neuronal firing and activity-dependent gene
282 transcription [31]. We therefore postulated that reduced BIN1 expression in human
283 glutamatergic neurons could affect Ca2+ dynamics, as previously suggested for
284 cardiomyocytes [32]. To directly test this possibility, we first studied Ca^{2+} dynamics in *BIN1*
285 WT and KO ASCL1-hiNs using real-time calcium imaging experiments. We observed
286 spontaneous synchronous calcium transients among adjacent cells both in *BIN1* WT and KO
287 ASCL1-hiNs cultures (Sup. Movies 3 and 4). By quantifying calcium spike transients (> 2
288 standard deviations above the noise level) we showed a significantly higher frequency of
289 Ca^{2+} transients in *BIN1* KO compared to WT ASCL1-hiNs (Fig. 8A,B and D). Moreover, the
290 dynamics of individual Ca^{2+} transients in *BIN1* KO were qualitatively different from WT
291 ASCL1-hiNs (Fig. 8C). These differences could be quantitatively measured by a longer time to
292 reach the maximum intracellular Ca^{2+} levels and to recover baseline levels (Fig. 8E-F).
293 In human heart failure, BIN1 expression is reduced, leading to an impairment in Cav1.2
294 trafficking, calcium transients, and contractility (Hong et al., 2012). Thus, we sought to
295 determine if BIN1 could also interact and regulate LVGCC expression in human neurons. To
296 that, we performed proximity ligation assay (PLA) to probe a possible interaction between

297 BIN1 and $Cav1_{.2}$ or $Cav_{1.3}$, the two LVGCCs expressed in ASCL1-hiNs (Sup. Fig. 5). We
298 observed a widespread BIN1-$Cav_{1.2}$ PLA signal (Fig. 8G) and, to a lesser extent, a BIN1-$Cav_{1.3}$
299 PLA signals in neurons (Sup. Fig. 5). Next, we quantified neuronal LVGCC protein by western
300 blotting and observed higher total $Cav_{1.2}$ expression in *BIN1* KO compared to WT ASCL1-hiNs
301 (Fig. 8H-I). Protein expression of neither $Cav_{1.3}$, nor the members of the Cav_2 family ($Cav_{2.1}$,
302 $Cav_{2.2}$ and $Cav_{2.3}$) were altered in the same cultures (Sup. Fig. 5), suggesting a specific
303 regulation of $Cav_{1.2}$ expression by BIN1.

304 Notably, LVGCCs are key regulators of neuronal firing [29] and activity-dependent
305 internalization of these channels is a key mechanism in firing homeostasis [33]. We thus set
306 out to investigate whether *BIN1* deletion could impair this mechanism in human neurons.
307 We stimulated ASCL1-hiNs with KCl 65nM for 30 min to induce neuronal depolarization and
308 collected total and endosomal proteins for analysis. We confirmed a higher global level of
309 $Cav_{1.2}$ in *BIN1* KO compared to WT ASCL1-hiNs that was independent of KCl treatment (Fig.
310 8J). However, $Cav_{1.2}$ expression in the endosomal fraction was 50% higher after KCl
311 treatment in *BIN1* WT, whereas this rise was only of 10% in *BIN1* KO ASCL1-hiNs (Fig. 8K).
312 This effect was specific for $Cav_{1.2}$ since both early endosome antigen 1 (EEA1) and $Cav_{1.3}$
313 expression rose in both *BIN1* WT and KO ASCL1-hiNs at similar levels after KCl treatment
314 (Fig. 8K). Altogether, these results indicate that BIN1 regulates activity-dependent
315 internalization and expression of $Cav_{1.2}$ in human neurons.

316

317 **Treatment with the calcium channel blocker nifedipine partly rescues electrical and**
318 **gene expression alterations in *BIN1* KO ASCL1-hiNs**

319 To investigate whether the network dysfunctions observed in *BIN1* KO ASCL1-hiNs may
320 be related to the higher expression of $Cav_{1.2}$, we treated these cells with a physiologically
321 relevant concentration (50nM) of the $Cav_{1.2}$ blocker nifedipine [34]) for 2 weeks and
322 recorded neuronal activity using MEA electrophysiology. We observed a partial recovery of
323 the oscillatory pattern of neuronal electrical activity observed in WT cells (Fig. 9A).
324 Interestingly, the percentage of spikes outside bursts was not affected by nifedipine
325 treatment in *BIN1* WT but was significantly lower in *BIN1* KO ASCL1-hiNs (Fig. 9B), indicating
326 a partial recovery of burst organization. To note, no difference in firing rates was observed
327 whatever the models and conditions (Fig. 9C). After 2 weeks of nifedipine treatment (4
328 weeks of differentiation), we also performed snRNA-seq experiments and recovered a total

329 of 1537 cells (n= 2 independent culture batches), which were mapped into the 7 clusters
330 described before (Fig. 4; Sup. Figure 6). Using Wilcoxon test, we found that nifedipine
331 treatment down-regulated several genes in *BIN1* KO ASCL1-hiNs, especially in the GluNeu-II
332 population (Sup. Table 6). Comparison of GO term enrichments between nifedipine-treated
333 and untreated *BIN1* KO vs WT GluNeu-II population revealed a consistent reduction of the
334 enrichment for several terms associated with ion channel activity and synapse transmission
335 in nifedipine-treated BIN1 KO cells (Figure 9D; Sup. Table 7). Altogether, these data support
336 the view that BIN1 contributes to the regulation of electrical activity and gene expression
337 through the regulation of $Cav_{1.2}$ expression/localization in human neurons.
338
339 **Molecular alterations in *BIN1* KO organoids and ASCL-hiNshiNs are also present in**
340 **glutamatergic neurons of the human brain at late stages of AD pathology**
341 We finally sought to evaluate whether molecular alterations in our neural models may
342 recapitulate some of those observed in the brain of AD cases. For this purpose, we used a
343 publicly available snRNA-seq dataset generated from the entorhinal cortex (EC) and superior
344 frontal gyrus (SFG) of AD patients at different Braak stages [35]. We first observed a
345 progressive and significant decrease in BIN1 mRNA levels in glutamatergic neurons (Fig.
346 10A), suggesting that reduced BIN1 expression in this cell type may be a common feature
347 occurring in the AD pathology progression. We then compared DEGs identified in BIN1 KO
348 glutamatergic neurons (either from COs or ASCL1-hiNs) with those identified in the same
349 cell subtype of AD brains (Sup. Table 8). Remarkably, DEGs identified in *BIN1* KO
350 glutamatergic neurons (either from COs or ASCL1-hiNs) showed a statistically significant
351 overlap with DEGs detected in this cell population in AD brains at different Braak stages (Fig.
352 10B). In astrocytes, however, a similar significant overlap could only be observed between
353 COs and AD brains (Fig. 10B). GO analysis based on DEG overlap between *BIN1* KO ASCL1-
354 hiNs and AD brain glutamatergic neurons indicated significant enrichment for pathways
355 associated with glutamate receptor activity and gated channel activity (Fig. 10C; Sup. Table
356 7). Similarly, DEG overlap between *BIN1* KO COs and AD brain glutamatergic neurons was
357 significantly enriched for genes associated with glutamate receptor activity, gated channel
358 activity and calcium ion binding (Fig. 10D; Sup. Table 7). No significant enrichment was
359 observed for DEG overlap between *BIN1* KO COs and AD brain astrocytes (data not shown).
360

361

362

363

364 ## Discussion

365

366 In this work, we show that the AD genetic risk factor *BIN1*, plays a critical role in the
367 regulation of neuronal firing homeostasis and gene expression in glutamatergic neurons.
368 Complete deletion of *BIN1* gene in these neurons is sufficient to alter the expression of the
369 LVGCC $Cav_{1.2}$, leading to altered calcium homeostasis and neural network dysfunctions in
370 human neurons *in vitro*. These functional changes are correlated with changes in the
371 expression of genes involved in synaptic transmission and ion transport across the
372 membrane, as well as elevated Tau phosphorylation. In long-term neuronal cultures using
373 COs, we show that reduced BIN1 expression is associated with fewer synapses and specific
374 gene expression alterations in glutamatergic neurons associated with activity-dependent
375 transcription. Notably, reduced BIN1 expression in human-induced glutamatergic neurons is
376 sufficient to elicit gene expression alterations that are also present in AD and converge to
377 biological processes related with calcium homeostasis. Together, our findings support the
378 view that altered BIN1 expression in glutamatergic neurons may contribute to AD
379 pathophysiology by dysregulating neuronal firing homeostasis via LVGCCs.

380 Neuronal network dysfunctions are observed in AD patients at early stages of the
381 disease and precede or coincide with cognitive decline [36–38]. Under physiological
382 conditions, neuronal networks can maintain optimal output through regulation of synaptic
383 plasticity and firing rate [39]. Our results suggest that normal levels of BIN1 expression in
384 glutamatergic neurons are fundamental to regulating neuronal firing rate homeostasis.
385 Accordingly, *BIN1* deletion in hiNs is sufficient to dysregulate network oscillations even
386 without impacting the number of functional synaptic contacts, suggesting that the
387 desynchronization observed in *BIN1* KO hiNs circuits are a consequence of disordered
388 homeostatic controls of neuronal activity. At later time-points (COs), glutamatergic neurons
389 show both gene expression alterations indicative of altered electrical activity and reduced
390 synaptic densities, which could indicate a synaptic down-scaling in response to earlier
391 augmented electrical activity (Dörrbaum et al., 2020).

392 One key mechanism controlling neuronal spiking activity is the regulation of Ca^{2+}
393 homeostasis [29,31,40]. Boosted neuronal electrical activity induces the turnover of LVGCCs
394 from the plasma membrane through endocytosis [33] and regulates the transcription of
395 genes encoding for calcium-binding proteins and calcium-mediated signaling [41],
396 mechanisms aiming to restore local Ca^{2+} signaling cascades and protect cells against
397 aberrant Ca^{2+} influx. We show that BIN1 interacts with $Cav_{1.2}$ in hiNs, similar to previous
398 findings in cardiac T tubules [32] and provide evidence supporting a novel role for BIN1 in
399 the regulation of activity-dependent internalization of $Cav_{1.2}$ in human neurons, thus linking
400 the known role of BIN1 in endocytosis [12] to firing homeostasis in human neurons via the
401 LVGCC. These results confirm in human neurons the interaction between endogenous
402 neuronal BIN1 and $Cav_{1.2}$ as previously suggested in mouse hippocampal neurons,
403 overexpressing a Bin1-mKate fused protein [18].
404 Loss of Ca^{2+} homeostasis is an important feature of many neurological diseases and
405 has been extensively described in AD [42,43]. Interestingly, DEGs identified in *BIN1* KO
406 glutamatergic neurons in our different cell culture models are enriched for calcium-related
407 biological processes. This is also observed for DEGs detected in glutamatergic neurons of the
408 AD brain at late stages of pathology when the expression levels of BIN1 in those cells is also
409 decreased. Thus, it is plausible to speculate that reduced expression of *BIN1* in
410 glutamatergic neurons may contribute to the breakdown of Ca^{2+} homeostasis in the AD
411 brain, potentially contributing to neuronal circuit dysfunctions. Consistent with this
412 hypothesis, we have previously shown a significant reduction in the expression of the
413 transcript encoding for the neuron-specific BIN1 isoform 1 in bulk RNA-sequencing data
414 from a large number of AD patients [7] and we show in this work that *BIN1* expression is
415 reduced in glutamatergic neurons of AD brains at late Braak stages. Moreover, it has been
416 recently shown that Bin1 conditional knockout in neurons and glial cells of the mouse
417 forebrain is sufficient to elicit gene expression changes associated with calcium-dependent
418 mechanisms (Ponnusamy et al., 2022), further supporting the interpretation that BIN1 plays
419 an important role in cellular processes involved in Ca^{2+} homeostasis in the brain.
420 Lastly, we show that treatment with the clinically approved calcium channel blocker
421 nifedipine for only 2 weeks is sufficient to partly recover electrical and gene expression
422 alterations in *BIN1* KO hiNs. These findings further support our interpretation that changes
423 in gene expression and electrical activity observed in *BIN1* HET and KO hiNs are a direct

424 consequence of reduced BIN1 expression in glutamatergic neurons and not a possible
425 artifact of CRISPR/Cas9 gene-editing in our hiPSC lines. Moreover, together with our
426 observations of reduced BIN1 expression and transcriptional alterations affecting biological
427 processes related to calcium homeostasis in human-induced glutamatergic neurons of the
428 human brain at late stages of AD pathology, our data strongly support a link between BIN1
429 and calcium homeostasis.

430 Thus, it is plausible to speculate that *BIN1* depletion in glutamatergic neurons
431 primarily undermines Ca^{2+} homeostasis, leading to changes in neuronal electrical activity. In
432 a later stage, gene expression and circuit-level alterations such as synapse loss would occur,
433 likely because of altered neuronal electrical activity. A corollary to this model would be that
434 early treatments aiming to restore Ca^{2+} homeostasis and neuronal electrical activity may
435 have a beneficial impact in AD onset and progression. Supporting this notion, both a
436 Mendelian randomization and a retrospective population-based cohort study found
437 evidence suggesting that treatment with Ca^{2+} channel blockers in human patients are
438 associated with a reduced risk of AD [44,45]. In the future, it would be interesting to study
439 the impact of these drugs for AD onset/progress as a function of genetic variants in the *BIN1*
440 locus.

441 An important limitation of our work is the absence of microglial cells in our models,
442 hampering the study of BIN1 roles in this cell type of high relevance to AD pathology [46].
443 However, our findings provide fundamental information about the molecular and cellular
444 processes impacted by reduced BIN1 expression in human neurons, which will require
445 further confirmation in the brain of patients carrying AD-related *BIN1* genetic variants.
446 Moreover, we studied the impact of heterozygous and knockout mutations, which do not
447 necessarily represent the consequences of AD-related *BIN1* genetic variants in gene
448 expression. Nevertheless, it is tempting to speculate that slight changes in *BIN1* expression
449 provoked by those variants could progressively deteriorate neuronal functions in the human
450 brain, contributing to AD pathogenesis in the elderly brain.
451

Declarations

Ethics approval and consent to participate

The datasets used and/or analysed during the current study are available from the corresponding author on reasonable request.

Consent for publication

Not applicable.

Availability of data and materials

Not applicable.

Competing interests

The authors declare no competing interests.

Funding

This work was co-funded by the European Union under the European Regional Development Fund (ERDF) and by the Hauts de France Regional Council (contract no.18006176), the MEL (contract_18006176), and the French State (contract no. 2018-3-CTRL_IPL_Phase2). This work was partly supported by the French RENATECH network (P-18-02737), Fondation pour la recherche médicale (ALZ201912009628, ALZ201906008477), PTR-MIAD, Fondation Recherche Alzheimer and by the Sanofi i-Awards Europe 2019. This work was also funded by the Lille Métropole Communauté Urbaine and the French government's LABEX DISTALZ program (Development of innovative strategies for a transdisciplinary approach to Alzheimer's disease). The UMR 8199 LIGAN-PM Genomics platform (Lille, France) belongs to the 'Federation de Recherche' 3508 Labex EGID (European Genomics Institute for Diabetes; ANR-10-LABX-46) and was supported by the ANR Equipex 2010 session (ANR-10-EQPX-07-01; 'LIGAN-PM'). The LIGAN-PM Genomics platform (Lille, France) is also supported by the FEDER and the Region Nord-Pas-de-Calais-Picardie and is a member of the "France Génomique" consortium (ANR-10-INBS-009).

483 **Authors' contributions**

484 Conceptualization, M.R.C.; Methodology, M.R.C., F.D., D.K., C.M.Q.; Investigation,
485 M.R.C., O.S., B.S.L., A.R.M.F., J.G., A.C., A.P., D.S.W., F.D., K.G., D.K., A.C.V., C.M.Q.; Writing -
486 Original Draft, M.R.C.; Writing - Reviews & Editing, M.R.C., F.D., J.C.L., C.M.Q., D.K.; Figures
487 preparation: M.R.C., F.D., A.P., B.S.L., A.R.M.F., D.K. Supervision, M.R.C., F.D., J.C.L., D.K.;
488 Funding Acquisition, M.R.C., J.C.L., F.D, D.K., P.A., A.B. All authors have read and approved
489 the manuscript.

490

491 **Acknowledgements**

492 The authors thank the BICeL platform of the Institut Biologie de Lille and the Vect'UB
493 viral platform (INSERM US 005 – CNRS 3427 – TBMCore, Université de Bordeaux, France).
494 The authors thank Karine Blary at the IEMN Lille for the microfabrication work. The Maestro
495 Pro multiwell microelectrode array was acquired with the "Prix Claude Pompidou pour la
496 Recherche sur l'Alzheimer (2021)" to MRC.

497

498

499 **References**

500 1. Lambert JC, Ibrahim-Verbaas CA, Harold D, Naj AC, Sims R, Bellenguez C, et al. Meta-
501 analysis of 74,046 individuals identifies 11 new susceptibility loci for Alzheimer's disease.
502 Nat Genet. Nature Publishing Group; 2013;45:1452–8.
503 2. Kunkle BW, Grenier-Boley B, Sims R, Bis JC, Damotte V, Naj AC, et al. Genetic meta-
504 analysis of diagnosed Alzheimer's disease identifies new risk loci and implicates Aβ, tau,
505 immunity and lipid processing. Nat Genet. Nature Publishing Group; 2019;51:414–30.
506 3. Schwartzentruber J, Cooper S, Liu JZ, Barrio-Hernandez I, Bello E, Kumasaka N, et al.
507 Genome-wide meta-analysis, fine-mapping and integrative prioritization implicate new
508 Alzheimer's disease risk genes. Nat Genet [Internet]. Springer US; 2021;53:392–402.
509 Available from: http://dx.doi.org/10.1038/s41588-020-00776-w
510 4. Bellenguez C, Küçükali F, Jansen IE, Kleineidam L, Moreno-Grau S, Amin N, et al. New
511 insights into the genetic etiology of Alzheimer's disease and related dementias. Nat Genet.
512 2022;54.
513 5. De Rossi P, Buggia-Prévot V, Clayton BLL, Vasquez JB, Van Sanford C, Andrew RJ, et al.
514 Predominant expression of Alzheimer's disease-associated BIN1 in mature oligodendrocytes
515 and localization to white matter tracts. Mol Neurodegener. BioMed Central Ltd.; 2016;11.
516 6. De Rossi P, Nomura T, Andrew RJ, Masse NY, Sampathkumar V, Musial TF, et al. Neuronal
517 BIN1 Regulates Presynaptic Neurotransmitter Release and Memory Consolidation. Cell Rep
518 [Internet]. ElsevierCompany.; 2020;30:3520-3535.e7. Available from:
519 https://doi.org/10.1016/j.celrep.2020.02.026
520 7. Marques-Coelho D, Iohan L da CC, Melo de Farias AR, Flaig A, Letournel F, Martin-Négrier
521 ML, et al. Differential transcript usage unravels gene expression alterations in Alzheimer's
522 disease human brains. npj Aging Mech Dis. Nature Research; 2021;7.
523 8. Glennon EBC, Whitehouse IJ, Miners JS, Kehoe PG, Love S, Kellett KAB, et al. BIN1 Is
524 Decreased in Sporadic but Not Familial Alzheimer's Disease or in Aging. PLoS One. 2013;8:1–
525 11.
526 9. Serrano-Pozo A, Frosch MP, Masliah E, Hyman BT. Neuropathological alterations in
527 Alzheimer disease. Cold Spring Harb Perspect Med. 2011;1:1–24.
528 10. Ubelmann F, Burrinha T, Salavessa L, Gomes R, Ferreira C, Moreno N, et al. Bin1 and CD
529 2 AP polarise the endocytic generation of beta-amyloid . EMBO Rep. 2017;18:102–22.
530 11. Miyagawa T, Ebinuma I, Morohashi Y, Hori Y, Chang MY, Hattori H, et al. BIN1 regulates

531 BACE1 intracellular trafficking and amyloid-β production. Hum Mol Genet. Oxford University
532 Press; 2016;25:2948–58.
533 12. Lambert E, Saha O, Soares Landeira B, Melo de Farias AR, Hermant X, Carrier A, et al. The
534 Alzheimer susceptibility gene BIN1 induces isoform-dependent neurotoxicity through early
535 endosome defects. Acta Neuropathol Commun [Internet]. 2022;10:4. Available from:
536 https://doi.org/10.1186/s40478-021-01285-5
537 13. Andrew RJ, De Rossi P, Nguyen P, Kowalski HR, Recupero AJ, Guerbette T, et al.
538 Reduction of the expression of the late-onset Alzheimer's disease (AD) risk-factor BIN1 does
539 not affect amyloid pathology in an AD mouse model. J Biol Chem [Internet]. NA;
540 2019;294:4477–87. Available from: http://dx.doi.org/10.1074/jbc.RA118.006379
541 14. Chapuis J, Hansmannel F, Gistelinck M, Mounier A, Van Cauwenberghe C, Kolen K V., et
542 al. Increased expression of BIN1 mediates Alzheimer genetic risk by modulating tau
543 pathology. Mol Psychiatry. 2013;18:1225–34.
544 15. Calafate S, Flavin W, Verstreken P, Moechars D. Loss of Bin1 Promotes the Propagation
545 of Tau Pathology. Cell Rep. Elsevier B.V.; 2016;17:931–40.
546 16. Jansen IE, van der Lee SJ, Gomez-Fonseca D, de Rojas I, Dalmasso MC, Grenier-Boley B,
547 et al. Genome-wide meta-analysis for Alzheimer's disease cerebrospinal fluid biomarkers.
548 Acta Neuropathol [Internet]. Springer Berlin Heidelberg; 2022;144:821–42. Available from:
549 https://doi.org/10.1007/s00401-022-02454-z
550 17. Schürmann B, Bermingham DP, Kopeikina KJ, Myczek K, Yoon S, Horan KE, et al. A novel
551 role for the late-onset Alzheimer's disease (LOAD)-associated protein Bin1 in regulating
552 postsynaptic trafficking and glutamatergic signaling. Mol Psychiatry. Nature Publishing
553 Group; 2019;
554 18. Voskobiynyk Y, Roth JR, Cochran JN, Rush T, Carullo NVN, Mesina JS, et al. Alzheimer's
555 disease risk gene BIN1 induces Tau-dependent network hyperexcitability. Elife. 2020;9:1–25.
556 19. Lancaster MA, Renner M, Martin CA, Wenzel D, Bicknell LS, Hurles ME, et al. Cerebral
557 organoids model human brain development and microcephaly. Nature [Internet]. Nature
558 Publishing Group; 2013;501:373–9. Available from: http://dx.doi.org/10.1038/nature12517
559 20. Trujillo CA, Gao R, Negraes PD, Gu J, Buchanan J, Preissl S, et al. Complex Oscillatory
560 Waves Emerging from Cortical Organoids Model Early Human Brain Network Development.
561 Cell Stem Cell [Internet]. Elsevier Inc.; 2019;25:558-569.e7. Available from:
562 https://doi.org/10.1016/j.stem.2019.08.002

563 21. Flavell SW, Greenberg ME. Signaling Mechanisms Linking Neuronal Activity to Gene
564 Expression and Plasticity of the Nervous System. Annu Rev Neurosci [Internet]. Annual
565 Reviews; 2008;31:563–90. Available from:
566 https://doi.org/10.1146/annurev.neuro.31.060407.125631
567 22. Tyssowski KM, DeStefino NR, Cho JH, Dunn CJ, Poston RG, Carty CE, et al. Different
568 Neuronal Activity Patterns Induce Different Gene Expression Programs. Neuron [Internet].
569 Elsevier Inc.; 2018;98:530-546.e11. Available from:
570 https://doi.org/10.1016/j.neuron.2018.04.001
571 23. Hrvatin S, Hochbaum DR, Nagy MA, Cicconet M, Robertson K, Cheadle L, et al. Single-cell
572 analysis of experience-dependent transcriptomic states in the mouse visual cortex. Nat
573 Neurosci [Internet]. 2018;21:120–9. Available from: https://doi.org/10.1038/s41593-017-
574 0029-5
575 24. Cortal A, Martignetti L, Six E, Rausell A. Gene signature extraction and cell identity
576 recognition at the single-cell level with Cell-ID. Nat Biotechnol. Nature Research; 2021;
577 25. Styr B, Slutsky I. Imbalance between firing homeostasis and synaptic plasticity drives
578 early-phase Alzheimer's disease. Nat. Neurosci. Nature Publishing Group; 2018. p. 463–73.
579 26. Harris SS, Wolf F, De Strooper B, Busche MA. Tipping the Scales: Peptide-Dependent
580 Dysregulation of Neural Circuit Dynamics in Alzheimer's Disease. Neuron [Internet]. Elsevier
581 Inc.; 2020;1–19. Available from: https://doi.org/10.1016/j.neuron.2020.06.005
582 27. Christopherson KS, Ullian EM, Stokes CCA, Mullowney CE, Hell JW, Agah A, et al.
583 Thrombospondins are astrocyte-secreted proteins that promote CNS synaptogenesis. Cell.
584 2005;120:421–33.
585 28. Love MI, Huber W, Anders S. Moderated estimation of fold change and dispersion for
586 RNA-seq data with DESeq2. Genome Biol. 2014;15:1–21.
587 29. Plumbly W, Brandon N, Deeb TZ, Hall J, Harwood AJ. L-type voltage-gated calcium
588 channel regulation of in vitro human cortical neuronal networks. Sci Rep. Nature Publishing
589 Group; 2019;9.
590 30. Marvin JS, Scholl B, Wilson DE, Podgorski K, Kazemipour A, Müller JA, et al. Stability,
591 affinity, and chromatic variants of the glutamate sensor iGluSnFR. Nat Methods. Nature
592 Publishing Group; 2018;15:936–9.
593 31. Simms BA, Zamponi GW. Neuronal voltage-gated calcium channels: Structure, function,
594 and dysfunction. Neuron. Cell Press; 2014. p. 24–45.

595 32. Hong TT, Smyth JW, Gao D, Chu KY, Vogan JM, Fong TS, et al. BIN1 localizes the L-type
596 calcium channel to cardiac T-tubules. PLoS Biol. 2010;8.
597 33. Green EM, Barrett CF, Bultynck G, Shamah SM, Dolmetsch RE. The Tumor Suppressor
598 eIF3e Mediates Calcium-Dependent Internalization of the L-Type Calcium Channel CaV1.2.
599 Neuron [Internet]. 2007;55:615–32. Available from:
600 https://linkinghub.elsevier.com/retrieve/pii/S0896627307005697
601 34. Hirasawa M, Pittman QJ. Nifedipine facilitates neurotransmitter release independently
602 of calcium channels. Proc Natl Acad Sci U S A. 2003;100:6139–44.
603 35. Leng K, Li E, Eser R, Piergies A, Sit R, Tan M, et al. Molecular characterization of
604 selectively vulnerable neurons in Alzheimer's disease. Nat Neurosci [Internet]. Springer US;
605 2021;24:276–87. Available from: http://dx.doi.org/10.1038/s41593-020-00764-7
606 36. Vossel KA, Beagle AJ, Rabinovici GD, Shu H, Lee SE, Naasan G, et al. Seizures and
607 Epileptiform Activity in the Early Stages of Alzheimer Disease. JAMA Neurol [Internet].
608 2013;70:1158–66. Available from: https://doi.org/10.1001/jamaneurol.2013.136
609 37. Vossel KA, Tartaglia MC, Nygaard HB, Zeman AZ, Miller BL. Review Epileptic activity in
610 Alzheimer's disease: causes and clinical relevance [Internet]. 2017. Available from:
611 www.thelancet.com/neurology
612 38. Lam AD, Deck G, Goldman A, Eskandar EN, Noebels J, Cole AJ. Silent hippocampal
613 seizures and spikes identified by foramen ovale electrodes in Alzheimer's disease. Nat Med
614 [Internet]. 2017;23:678–80. Available from: https://doi.org/10.1038/nm.4330
615 39. Turrigiano GG, Nelson SB. Homeostatic plasticity in the developing nervous system. Nat
616 Rev Neurosci. 2004;5:97–107.
617 40. Frere S, Slutsky I. Alzheimer's Disease: From Firing Instability to Homeostasis Network
618 Collapse. Neuron. Cell Press; 2018. p. 32–58.
619 41. Dörrbaum AR, Alvarez-Castelao B, Nassim-Assir B, Langer JD, Schuman EM. Proteome
620 dynamics during homeostatic scaling in cultured neurons. Elife. eLife Sciences Publications
621 Ltd; 2020;9.
622 42. Bezprozvanny I, Mattson MP. Neuronal calcium mishandling and the pathogenesis of
623 Alzheimer's disease. Trends Neurosci [Internet]. Elsevier; 2008;31:454–63. Available from:
624 https://doi.org/10.1016/j.tins.2008.06.005
625 43. Carvalho LI, Lambert J-C, Costa MR. Analysis of modular gene co-expression networks
626 reveals molecular pathways underlying Alzheimer's disease and progressive supranuclear

627 palsy. medRxiv [Internet]. 2021;2021.09.21.21263793. Available from:
628 http://medrxiv.org/content/early/2021/10/05/2021.09.21.21263793.1.abstract
629 44. Ou YN, Yang YX, Shen XN, Ma YH, Chen SD, Dong Q, et al. Genetically determined blood
630 pressure, antihypertensive medications, and risk of Alzheimer's disease: a Mendelian
631 randomization study. Alzheimer's Res Ther. Alzheimer's Research & Therapy; 2021;13:1–9.
632 45. Wu CL, Wen SH. A 10-year follow-up study of the association between calcium channel
633 blocker use and the risk of dementia in elderly hypertensive patients. Med (United States).
634 2016;95.
635 46. Nott A, Holtman IR, Coufal NG, Schlachetzki JCM, Yu M, Hu R, et al. Brain cell type–
636 specific enhancer–promoter interactome maps and disease-risk association. Science (80-).
637 American Association for the Advancement of Science; 2019;366:1134–9.
638 47. Wagenaar DA, Pine J, Potter SM. An extremely rich repertoire of bursting patterns
639 during the development of cortical cultures. BMC Neurosci. 2006;7:1–18.
640 48. Hao Y, Hao S, Andersen-Nissen E, Mauck WM, Zheng S, Butler A, et al. Integrated
641 analysis of multimodal single-cell data. Cell [Internet]. Elsevier Inc.; 2021;184:3573-
642 3587.e29. Available from: https://doi.org/10.1016/j.cell.2021.04.048
643 49. Korotkevich G, Sukhov V, Sergushichev A. Fast gene set enrichment analysis. bioRxiv.
644 BioAr. 2019;
645
646

647 **Figure legends**

648 **Figure 1: Similar transcriptional changes in glutamatergic neurons from 6.5-month-**
649 **old *BIN1* HET and KO COs.** (A) Scheme of the experimental design. (B) UMAP representation
650 of the different cell subtypes in COs identified using snRNA-seq. (C) Dot plot representing
651 the expression for *BIN1* and key markers used to annotate cell subtypes. (D) Proportion of
652 cell subpopulations in the three genotypes (****p<0.0001; Chi-squared test). (E) Volcano
653 plots representing DEGs comparing HET vs WT or KO vs WT in astrocytes and glutamatergic
654 neurons. DEGs with adjusted p-value <0.05 and |log2FC| >0.25 are shown in red. (H)
655 Functional enrichment analysis of DEGs commonly identified in HET and KO glutamatergic
656 neurons. GO: gene ontology; BP: biological processes; CC: cellular components; MF:
657 molecular function.

658

659 **Figure 2: Altered expression of activity-related genes in BIN1 HET and KO**
660 **glutamatergic neurons**. (A) Scheme indicating the different sets of ARGs regulated by brief
661 and sustained patterns of electrical activity [22,23]. rPRGs: rapid primary response genes;
662 dPRGs: delayed primary response genes; SRGs: secondary response genes; ERGs: early
663 response genes; LRGs: late response genes; Exc – glutamatergic neurons; Inh – GABAergic
664 neurons. (B) Feature plots showing the enrichment score of single cells for ARG signatures.
665 Enrichment scores correspond to the $-\log10(p_{adj})$ of the Cell-ID-based enrichment test. (C)
666 Proportions of glutamatergic neurons (right) enriched for the different ARG signatures
667 according to genotype (*p<0.05; **p<0.01; ***p<0.001; Chi-squared test).

668

669 **Figure 3: Reduced synaptic numbers in BIN1 HET and KO cerebral organoids.** (A)
670 Immunohistochemistry for HOMER1 (red), SYP (green) in 6.5-month-old *BIN1* WT, HET and
671 KO COs. Insert (A') illustrates the identification of putative synaptic contacts. (B-D)
672 Quantifications of the SYP and HOMER1 spot density, and the percentage of SYP assigned by
673 HOMER1 spots in *BIN1* WT, HET and KO COs ($^{\#}$p<0.1; *p<0.05; **p<0.01; Dunn's multiple
674 comparison test; n=3 COs per genotype). (E) Western blot for total TAU protein C-terminal
675 (TAU-C), phosphorylated (p)-TAU at Ser202, Thr205 (AT8) and β-ACTIN in 6.5-month-old
676 COs. (F-H) Quantification of TAU-C/β-ACTIN, p-TAU/β-ACTIN and p-TAU/TAU-C levels
677 normalized to WT ($^{\#}$p<0.1; Mann-Whitney test; n=3 COs per genotype). (I) Western blot for

678 APP and β-ACTIN in 6.5-month-old COs. (J-L) Quantification of APP/β-ACTIN, β-CTF/β-ACTIN
679 and β-CTF /APP levels normalized to WT (n=3 COs per genotype).
680
681 **Figure 4: Neuronal-specific BIN1 KO cell-autonomously elicit transcriptional changes.**
682 (A) Scheme of the Ascl1-induced hiNs experiments. (B) Images showing BIN1 WT and KO
683 hiNs 7 days after the beginning of doxycycline treatment immunolabeled for neuronal
684 markers MAP2 and TUBB3 and astrocyte marker GFAP and stained with DAPI. (C) UMAP
685 representation of the different cell subtypes identified in ASCL1-hiNs cultures using snRNA-
686 seq. (D) Dot plot representing expression of key markers used to annotate cell subtypes. (E)
687 Volcano plot representing DEGs comparing BIN1 KO vs WT glutamatergic neurons (GluNeu-
688 II). Differential expression analysis was performed using DEseq2 on the sample level gene
689 expression matrix, including the experiment batch as covariates. DEGs with adjusted p-value
690 <0.05 and |log2FC| >0.25 are shown in red. Gene labels are shown for calcium- and
691 synapse-related genes. (F) Functional enrichment analysis of DEGs identified in
692 glutamatergic neurons. Bar plots representing the top 15 the enriched GO terms in each
693 category at adjusted p-value <0.01. (G) UMAP representing GluNeu-II enrichment for
694 delayed Primary Response Genes (dPRGs) and Secondary Responses Genes (SRGs)
695 (Tyssowski et al., 2018). Red point indicate enrichment with adjusted p-value<0.05,
696 hypergeometric test using CellID. (H) Barplot of the percentage of enriched GluNeu-II cells
697 by genotype for each gene sets.
698
699 **Figure 5: *BIN1* KO ASCL-hiNs have a higher spike burst frequency compared to WT.**
700 (A) Raster plots showing MUA recorded for 1 minute in *BIN1* WT and KO ASCL1-hiNs after 4
701 weeks of differentiation. Each line represents one electrode localized side-by-side in our
702 microfluidic/MEA array (as in panel A). (B-C) Quantification of the number of detected
703 spikes at different time points (*p=0.0141; ***p=0.0006; Two-way ANOVA followed by
704 Tukey's multiple-comparison test; n= 5 for each genotype). (D) Quantification of the number
705 of spike bursts at different time points (**p=0.004; $^{\#}$p=0.0888; Mann-Whitney test).
706
707 **Figure 6: Disorganization of neuronal activity in *BIN1* KO ASCL1-hiNs.** (A) Raster plots
708 showing the decomposition of multi-unity activity (MUA, black lines) into single-unit activity
709 (SUA, colored lines) using spike waveform clustering. (B-E) Quantification of single-neuron

710 firing rate (B; **p=0.0034), spike amplitude (C; *p=0.0106), burst duration (D;
711 ****p<0.0001) and number of spikes per burst (E; ****p<0.0001) at 4 weeks. Mann-
712 Whitney test; n= 5 independent experiments; WT: 376 neurons; KO: 416 neurons). (F) Raster
713 plots showing SUA recorded from 5 different electrodes of *BIN1* WT (left) or KO (right) ASCL-
714 hiNs cultures after 4 weeks of differentiation. (G) Array-wide spike detection rate (ASDR)
715 plots based on SUA recorded in *BIN1* WT and KO ASCL1-hiNs cultures. Each line represents
716 one independent culture batch. (H-I) Normalized autocorrelogram heatmap (H, each line
717 refers to one SUA) and averaged correlation (I) for all SUAs recorded in 5 independent *BIN1*
718 WT and KO ASCL1-hiNs cultures. (J) Percentage of spikes outside of bursts (*p=0.0417,
719 Mann-Whitney test).
720
721 **Figure 7: Similar synaptic density and higher TAU phosphorylation in *BIN1* KO**
722 **compared to WT ASCL1-hiNs.** (A-B) Immunocytochemistry using the astrocyte marker GFAP,
723 neuronal marker MAP2, pre-synaptic marker SYP and post-synaptic marker HOMER1 in *BIN1*
724 WT ASCL1-hiNs after 4 weeks of differentiation in a three-chamber microfluidic device. Scale
725 bar = 200 µm. Rectangular box in A is magnified in B, allowing the identification of putative
726 synaptic contacts. (C-D) Fraction of SYP spots assigned by HOMER1 spots in MAP2 processes
727 at 4 (C) and 6 weeks (D) ASCL1-hiNs cultures (n= 8 independent devices for each genotype).
728 (E) Western blot for total TAU protein C-terminal (TAU-C), phosphorylated (p)-TAU at
729 Ser202, Thr205 (AT8) and β-ACTIN in 4-week-old ASCL1-hiNs cultures. (F) Quantification of
730 TAU-C/β-ACTIN and p-TAU/TAU-C levels in BIN1 KO ASCL1-hiNs normalized to WT
731 (*p=0.0262; Mann-Whitney test).
732
733 **Figure 8: Altered frequency of calcium transients in *BIN1* KO ASCL1-hiNs.** (A)
734 Snapshot of a 4-week-old ASCL1-hiNs culture labeled with Oregon green BAPTA. (B)
735 Representative plot of fluorescence change over time in 1000 frames. (C) Representative
736 traces showing the fluorescence changes in *BIN1* WT and KO ASCL1-hiNs. Red dashed lines
737 indicate the time to reach the fluorescence maximal intensity (raising time - t1) and to
738 return to baseline (recovery time - t2). (D) Quantification of calcium transients in *BIN1* WT
739 and KO ASCL1-hiNs (****p<0.0001; Mann-Whitney test; n= 3 independent cultures for each
740 genotype; number of active cells per condition: 754 (WT), 1006 (KO)). (E-F) Quantification of
741 rising time (t1) and recovery time (t2) for calcium transients (**p=0.0022; ****p<0.0001;

742 Mann-Whitney test). (G) Images showing PLA spots using anti-BIN1 and anti-$Cav_{1.2}$
743 antibodies in 4-week-old *BIN1* WT and KO hiNs. Cells were also immunolabeled for the
744 neuronal marker MAP2 (green), the astrocyte marker GFAP (white), and stained with DAPI
745 (blue). (H) Western blot for Cav1.2 (without and with blocking peptide) and β-ACTIN in 4-
746 week-old ASCL1-hiNs cultures. (I) Quantification of Cav1.2/β-ACTIN levels in *BIN1* WT and
747 KO ASCL1-hiNs cultures (*p=0.0286; Unpaired t-test). (J) Western blot for $Cav_{1.2}$ and β-ACTIN
748 in the total protein extracts from 4-week-old ASCL1-hiNs treated with KCl (+) or vehicle (-).
749 Plot shows the quantification of $Cav_{1.2}$ normalized by β-ACTIN. (K) Western blot for $Cav_{1.2}$,
750 $Cav_{1.3}$ and EEA1 in the endosomal protein extracts from 4-week-old ASCL1-hiNs treated with
751 KCl (+) or vehicle (-). Plot shows the optical density of these proteins (****p<0.0001; Chi-
752 square test).
753
754 **Figure 9: Nifedipine treatment partly rescues electrical and gene expression**
755 **alteration in BIN1 KO hiNs.** (A) Auto-correlograms of 4-week-old *BIN1* WT and KO hiNs
756 treated or not with 50 nM Nifedipine for 2 weeks. (B) Percentage of spikes outside of bursts
757 (WT vs WT+NIF: **p_{adj}=0.0034; WT vs KO: *p_{adj}=0.0124; Dunn's multiple comparison test).
758 (C) Average firing rates. (D) Comparison of the enrichment for GO terms in genes
759 upregulated in KO vs WT and KO + nifedipine (NIF) vs WT GluNeu-II using fast gene set
760 enrichment analysis (FGSEA). The FGSEA results are shown for the top15 GO terms with
761 reduce enrichment in KO NIF.
762
763 **Figure 10: Similar molecular alterations in *BIN1* KO hiNs and glutamatergic neurons**
764 **of the AD brain.** (A) Box plot representing *BIN1* mRNA in expression through different Braak
765 stages in entorhinal cortex (EC) and superior frontal gyrus (SFG) (***p_{adj}<0.001; Wilcoxon
766 test). (B) Dot plot representing the overlap between DEGs identified in glutamatergic
767 neurons of the AD brain and *BIN1* KO ASCL1-hiN cultures (left) or *BIN1* KO COs (right). (C-D)
768 Network representation of enriched GO terms in overlapping DEGs between AD brains and
769 glutamatergic neurons in culture. Enriched GO terms were identified using over-
770 representation test.
771
772
773

774
775
776
777
778 **Supplementary data**

779 **Sup. Figure 1: Cellular and molecular characterization of 6.5-month-old cerebral**
780 **organoids.** (A) Immunohistochemistry for GFAP (red), MAP2 (green) and DAPI (blue) in 6.5-
781 month-old *BIN1* WT, HET and KO COs. (B) Western blots showing the isoforms of BIN1
782 detected in WT, WT, the reduced expression in HET, and the absence of BIN1 protein in KO
783 COs. (C) Western blots showing the expression of neuronal (TAU and vGLUT2) and astrocytic
784 (GFAP) proteins in 14 individual COs at 190 days, including some of the BIN1 WT, HET and
785 KO samples used for snRNA-seq. Note the low variability in protein expression. (D) Volcano
786 plots representing DEGs comparing HET vs WT or KO vs WT in astrocytes and glutamatergic
787 neurons. DEGs with adjusted p-value <0.05 and |log2FC| >0.25 are shown in red. Gene
788 labels are shown for top 10 genes in terms of log2FoldChange and p-value. (E) (H) Functional
789 enrichment analysis showing the top 15 significantly enriched GOs for DEGs identified in the
790 *BIN1* KO vs WT or HET vs WT glutamatergic neurons. GO: gene ontology; BP: biological
791 processes; CC: cellular components; MF: molecular function.
792

793 **Sup. Figure 2: Reduced BIN1 expression does not enhance activity-dependent**
794 **transcription in GABAergic neurons**. A-B) Proportions of GABAergic neurons enriched for
795 the different ARG signatures according to genotype (*p<0.05; **p<0.01; ***p<0.001; Chi-
796 squared test).
797

798 **Sup. Figure 3: Normal glutamatergic transmission in *BIN1* KO ASCL1-hiNs**. Box plots
799 show the number of active spots per neuron and number of events detected by time-lapse
800 video-microscopy in 4- or 6-week-old ASCL1-hiNs cultures transduced with the glutamate
801 sensor iGLUSnFr (4 weeks: n= 378 BIN1 WT and 266 BIN1 KO ASCL1-hiNs; 6 weeks: n= 685
802 BIN1 WT and 629 BIN1 KO ASCL1-hiNs).
803

804 **Sup. Figure 4: Normal APP processing in *BIN1* KO ASCL1-hiNs**. (A) Western blots
805 showing the expression of APP full-length, β-CTF and β-ACTIN at 4 weeks. (B) Quantification

806 of the ratios APP/β-ACTIN, β-CTF /β-ACTIN and β-CTF/APP (n = 5 for each genotype). (C)
807 Quantification of soluble A$\beta_{1\text{-}x}$, A$\beta_{1\text{-}42}$ and the ratio A$\beta_{1\text{-}42}$/ A$\beta_{1\text{-}x}$ in ASCL1-hiNs cultures at 3
808 and 4 weeks.
809
810 **Sup. Figure 5: Expression of voltage-gated calcium channels in ASCL1-hiNs**. (A) Violin
811 plots showing the mRNA levels of Cav1 and Cav2 members of the voltage-gated calcium
812 channel families L-type, P/Q-type, N-type and R-type detected in ASCL1 hiNs. (B) Images
813 showing PLA spots using anti-BIN1 and anti-Cav1.3 antibodies in 4-week-old *BIN1* WT hiNs.
814 Cells were also immunolabeled for the neuronal marker MAP2 (green), the astrocyte marker
815 GFAP (white), and stained with DAPI (blue). (C) Western blots showing the expression of
816 Cav1.3, Cav2.1, Cav2.2, Cav2.3 and β-ACTIN in 4-week-old ASCL1h hiNs. (D) Quantification of
817 protein expression.
818
819 **Sup. Figure 6: snRNAseq of nifedipine treated ASCL1-hiNs cultures**. (A) UMAP of the
820 n=2 nifedipine experiments integrated with the other hiNs snRNA-seq experiments. (B)
821 correlation between the differential gene expression in untreated *BIN1* KO + vehicle vs WT
822 (x axis, DEGs are plotted in red) and in *BIN1* KO + nifedipine (nif) vs WT. Calcium- and
823 synapse-related genes upregulated in *BIN1* KO + vehicle vs WT are labeled if the genes are
824 not upregulated in KO + nif vs WT. (C) Plot showing the total number of DEGs identified in
825 *BIN1* KO ASCL1-hiNs treated or not with nifedipine.
826
827 **Sup. Movies 1 and 2:** Time-series of 1000 frames taken from *BIN1* WT and KO ASCL1-
828 hiNs transduced with iGLUSnFr after 2 weeks of differentiation and imaged 2 weeks later.
829 Videos are played at 100 fps.
830
831 **Sup. Movies 3 and 4:** Time-series of 1000 frames taken from *BIN1* WT and KO ASCL1-
832 hiNs after 4 weeks of differentiation and labeled with Oregon Green BAPTA and imaged.
833 Videos are played at 100 frames per second (fps).
834
835 **Sup. Table 1:** DEGs identified in different cell types/subtypes of COs.
836

837 **Sup. Table 2:** GO terms enriched for DEGs identified in different cell types/subtypes of
838 COs.
839
840 **Sup. Table 3:** List of ARGs used for hypergeometric test in Cell-ID.
841
842 **Sup. Table 4:** DEGs identified in different cell types/subtypes of ASCL1-hiNs cultures.
843
844 **Sup. Table 5:** GO terms enriched for DEGs identified in different cell types/subtypes of
845 ASCL1-hiNs cultures.
846
847 **Sup. Table 6:** DEGs identified in different cell types/subtypes of ASCL1-hiNs cultures
848 treated with nifedipine.
849
850 **Sup. Table 7:** GO terms enriched for DEGs identified in different cell types/subtypes of
851 ASCL1-hiNs cultures treated with nifedipine.
852
853 **Sup. Table 8:** DEGs identified in different cell types/subtypes of the AD brain.
854
855 **Sup. Table 9:** GO terms enriched for DEGs commonly identified in *BIN1* HET or KO cells
856 and the AD brain.
857
858
859
860
861
862
863
864
865
866
867
868

869
870
871
872
873
874 **Materials and methods**
875
876 *Maintenance of isogenic hiPSC lines and neural induction*
877 Isogenic hiPSCs (ASE 9109, Applied StemCell Inc. CA, USA) modified for BIN1 in exon 3
878 were generated by CRISPR/Cas9. Homozygous null mutants for BIN1 had a 5 bp deletion on
879 one allele and an 8 bp deletion on the other allele. Heterozygous for BIN1 had a 1bp
880 insertion on one allele. All hiPSCs, and all subsequent human induced neural progenitor cells
881 (hiNPCs), hiNs, human induced astrocytes (hiAs), and cerebral organoids derived thereof,
882 were maintained in media from Stemcell Technologies, Vancouver, Canada. Maintenance of
883 cell cultures and organoids were done in adherence with manufacturer's protocols which
884 can be found on the webpage of Stemcell Technologies. hiPSCs were maintained in mTeSR1
885 medium in non-treated cell culture dishes/plates pre-coated with vitronectin. Cell numbers
886 and viability were recorded using a LUNA™ Automated Cell Counter.
887 To generate *BIN1* WT and KO hiNPCs, we used the dual SMAD-inhibition (SMADi)
888 method (Chambers et al., 2009). Briefly, hiPSCs are cultured and passaged for 3 times in
889 STEMdiff™ Neural Induction Medium + SMADi (Stemcell Technologies) for up to 3 weeks.
890 After this period, hiNPCS are maintained for up to 10 passages in treated cell culture dishes
891 pre-coated with poly-L-ornithine (PLO) and laminin (5 µg/mL), using STEMdiff™ Neural
892 Progenitor Medium (NPM; Stemcell Technologies). PLO solution was made in water
893 (0.001%) while laminin was diluted in PBS with Ca2+ and Mg2+.
894
895 *Generation of Cerebral Organoids*
896 Cerebral organoids (3D Cultures) were generated from *BIN1* WT, HET and KO hiPSCs
897 using a 4-stage protocol (Lancaster et al., 2013). The first step was the Embryoid Body (EB)
898 Formation Stage, where hiPCSc at 80%-90% confluency were detached from the Vitronectin
899 XF substrate using Accutase (#AT-104, Innovative Cell Technologies). To form the EB, 9000
900 cells were plated per well in a 96-well round-bottom ultra-low attachment plate containing

901 EB seeding medium (Stem Cell Technologies). At day 2 and day 4, EB formation media is
902 added in the wells. After five days, the EBs were transferred to a 24-well ultra-low
903 attachment plate containing Induction Medium (Stem Cell Technologies), where each well
904 receives 1-2 EBs. Two days later, the EBs were ready for the Expansion Stage. The EBs were
905 embedded in Matrigel (Corning) and transferred to a 24-well ultra-low adherent plate with
906 Expansion Medium (Stem Cell Technologies). After three days, the medium was replaced by
907 Maturation Medium (Stem Cell Technologies) and the plate was placed in an orbital shaker
908 (100 rpm speed). During this final Maturation Phase, 75% medium change was done on a
909 biweekly basis. Organoids were allowed to mature for a period of 6.5 months.
910
911 *Generation of pure human neuronal cultures from hiNPCs*
912 We differentiated neurons from virus-transduced hiNPCs according to an adapted
913 protocol (Zhang et al., 2013; Yang et al., 2017). Briefly, hiNPCs are first virally-transduced
914 with the TTA lentiviral construct and a passage later, the TetO-Ascl1-Puro lentiviral construct
915 was transduced. These cells are maintained in NPM medium and expanded prior to
916 differentiation. For differentiation of human induced neurons (hiNs), hiNPCs are plated onto
917 PLO/laminin-coated imaging plates at density 100,000 cells/well in NPM. After 24 h,
918 complete BrainPhys medium (StemCell Technologies) is added 1:1 together with 2 µg/mL
919 doxycycline (Sigma-Aldrich) to induce TetO gene expression. The following day, 1 µg/mL
920 puromycin (Sigma-Aldrich) was added to start cell selection. After 2-3 days (depending on
921 the efficiency of antibiotic selection), 50,000 human cortical astrocytes were added in each
922 well with BrainPhys containing doxycycline. After 24 h, 2 µM of Ara-C (Cytosine β-D-
923 arabinofuranoside; Sigma-Aldrich) was added to arrest the proliferation of astrocytes. Half
924 of the medium in each well was changed biweekly with fresh BrainPhys medium containing
925 doxycycline until the 14th day. After that, the biweekly medium change was performed only
926 with BrainPhys. Differentiation was allowed to continue for another 2-4 weeks prior to
927 subjecting the cells to various experimental manipulations. Human cortical astrocytes (HA;
928 ScienCell # 1800) were sourced from ScienCell Research Laboratories, CA, USA and grown up
929 to 10 passages on poly-l-lysine coated 75 cm^2 flasks using astrocyte medium (ScienCell #
930 1801) supplemented with astrocyte growth supplement (AGS, ScienCell #1852) and 10 ml of
931 fetal bovine serum (ScienCell # 1800).

932 This co-culture system was characterized using snRNA-seq after 4 weeks of
933 differentiation showing that 70% of cells (n=7120 from 5 independent culture batches)
934 expressed the pan-neuronal markers SOX11, SNAP25, DCX and RBFOX3, with 66% of cells
935 co-expressing the glutamatergic neuron marker SLC17A6, less than 1.5% of cells co-
936 expressing the GABAergic neuron markers DLX1, GAD1 and GAD2, and 5% of cells co-
937 expressing low levels of markers of both neuronal subtypes. The remaining cells, immature
938 astrocytes (Astro-I), mature astrocytes (Astro-II) and undifferentiated NPCs, represented
939 about 15%, 8%, 4% of the cells, respectively. The first two cell populations likely represent
940 two different states of astrocytes added to the cultures, whereas NPCs are likely cells that
941 failed to reprogram into hiNs despite ASCL1 transduction. Thus, neuronal classes generated
942 in this system comprise a large fraction of glutamatergic neurons (84%), a small proportion
943 of GABAergic neurons (2.5%) and unspecified neurons co-expressing low levels of markers
944 of both neuronal subtypes (13.5%).
945
946 *Culture of hiNs in Microfluidic Devices*
947 Three-compartment microfluidic neuron culture devices were used in which the
948 presynaptic and postsynaptic chambers are connected to the synaptic chamber by
949 respectively long and short micro-channels. Details of the microfluidic device design and
950 fabrication have been previously described (Kilinc et al, 2020).
951 The homemade devices were placed individually in Petri dishes for easy handling and
952 UV sterilized for 30 min before coating for cell adhesion. The primary surface coating
953 consisted of poly-L-lysine (Sigma-Aldrich) at 20 µg/mL in borate buffer (0.31% boric acid,
954 0.475% sodium tetraborate, pH 8.5). All coated devices were incubated overnight at 37°C,
955 5% CO2. After a wash with DPBS, devices were then coated with 20 µg/mL laminin in DPBS
956 and incubated overnight at 37°C in 5% CO2. The following day, devices were carefully
957 washed once with DPBS before cell plating.
958 In total, 30,000 hiNPCs resuspended in NPM containing 10 µM of Y-27632 ROCK
959 inhibitor were seeded per device, half at the entrance of the presynaptic somatic chamber
960 and half at the entrance of the postsynaptic somatic chamber. Microfluidic devices were
961 microscopically checked at the phase contrast to ensure the cells were correctly flowing into
962 chambers. After a minimum of 5 minutes to allow the cells to attach, devices were filled
963 with NPM (containing 10 µM of Y-27632 ROCK Inhibitor). Water was added to the Petri

964 dishes to prevent media evaporation, and these were then incubated at 37°C in a humidified
965 5% CO2 incubator. For induced neuron culture from hiNPCs transduced for Ascl1,
966 doxycycline (2 µg/mL) was added on the first day of half medium change to induce TetO
967 gene expression. The following day, puromycin (1 µg/mL) was added to start cell selection.
968 Two days after the puromycin selection, a total of 5,000 HAs (ScienCell Research
969 Laboratories, CA, USA) were added per device. After 24 hours, Ara-C (2 µM) was added to
970 stop their proliferation. Half of the medium was changed twice a week with complete
971 BrainPhys medium + 2 µg/mL doxycycline for 14 days. After that, half medium change was
972 performed only with BrainPhys medium.
973 Five microfluidic devices were employed for each experimental condition (*BIN1* KO vs
974 WT both for spontaneous neuronal differentiation and Ascl1 induction) and two
975 independent cultures were performed. To assess the time-course effect, neuron cultures
976 were stopped at 4 and 6 weeks.
977
978 *Viral Transductions*
979 Lentiviral constructs were produced by the Vect'UB platform within the TBM Core unit
980 at University of Bordeaux, Bordeaux, France (CNRS UMS 3427, INSERM US 005). The
981 lentiviral constructs used were TTA (Vect'UB; ID # 571) and TetO-Ascl1-Puro (Addgene, #
982 97329). Lentiviral infections were done in NPCs at P3 or P4. The viral constructs were
983 transduced at a multiplicity of infection (MOI) of 2.5. In brief, NPCs were plated at a
984 confluency of 1x106 cells per well of a 6-well plate. After 4 hours of plating the cells,
985 appropriate volumes of each lentiviral construct were mixed in complete Neural Progenitor
986 medium and 50 µl of the viral medium mix was then added to each well. We transduced the
987 TTA construct at first in the hiNPCs. Following one passage, the TTA-transduced cells were
988 transduced with the construct for ASCL1. Cells having both viral constructs were then
989 further expanded for 1 or 2 passages before being used for differentiation into hiNs.
990 The iGluSnFR construct was an adeno-associated viral vector (BS11-COG-AAV8)
991 sourced from Vigene Biosciences, MD, USA. The viral construct was transduced at a MOI of
992 5,000 at around 10 days of differentiation for the ASCL1-hiNs. Differentiation was allowed to
993 continue for a duration of 4-6 weeks prior to MEA electrophysiology or imaging.
994
995 *Immunocytochemistry and Immunohistochemistry*

996 Bidimensional (2D) cultures: All cells were fixed in 4% (w/v) paraformaldehyde
997 (Electron Microscopy Sciences, Catalog # 15712) for 10 minutes in the imaging plates.
998 Following, fixation, cells were washed thrice with PBS 0.1 M. Blocking solution (5% normal
999 donkey serum + 0.1% Triton X-100 in PBS 0.1 M) was added to fixed cells at room
1000 temperature for 1 hour under shaking conditions. After the blocking step, primary
1001 antibodies were added to cells in the blocking solution and incubated overnight at 4°C. The
1002 following day, cells were washed with PBS 0.1 M thrice for 10 mins. Each. Alexa Fluor®--
1003 conjugated secondary antibodies in blocking solution were then incubated with the cells for
1004 2 hours at room temperature under shaking conditions ensuring protection from light.
1005 Subsequently, 3 washes with 0.1 M PBS were done for 10 min each at room temperature
1006 under shaking conditions with protection from light. Hoechst 33258 solution was added
1007 during the second PBS wash. Cells were mounted with Aqua-Poly/Mount (Polysciences, Inc.)
1008 and imaged directly in the cell imaging plates. All images were acquired using an LSM 880
1009 Confocal Scanning Microscope housed at the Imaging Platform of the Pasteur Institute, Lille.
1010 Duolink® Proximity Ligation Assays (PLA) was used to detect endogenous Protein-Protein
1011 Interactions. The following pairs of antibodies were used: anti-BIN1 (rabbit, 182562, abcam)
1012 and anti-Cav1.2 (mouse, 84814, abcam); or anti-BIN1 and anti-Cav1.3 (mouse, 85491,
1013 mouse). Other antibodies used for immunocytochemistry were: MAP2 (188006 and
1014 188004, Synaptic Systems), Beta III Tubulin (MAB1637, Sigma-Aldrich), GFAP (AB5804,
1015 Millipore; and 173006, Synaptic Systems). All Alexa Fluor®-tagged secondary antibodies
1016 were sourced from Jacskon ImmunoResearch Europe Ltd.
1017 Microfluidic Devices: Cultured induced neurons were fixed in 4% paraformaldehyde in
1018 PBS for 15 min at room temperature, washed three times with PBS, and permeabilized with
1019 0.3% Triton X-100 in PBS for 5 min at room temperature. Cells were blocked in PBS
1020 containing 5% normal donkey serum for 1 h at room temperature before overnight
1021 incubation at 4°C with the following primary antibodies: MAP2 (188006, Synaptic Systems);
1022 HOMER1 (160004, Synaptic Systems), Synaptophysin (101011, Synaptic Systems), and GFAP
1023 (AB5804, Millipore). Cells were washed twice with PBS and incubated with the following
1024 secondary antibodies for 2h at room temperature: DyLight™ 405 Donkey Anti-Chicken (703-
1025 475-155, Jackson ImmunoResearch), Alexa Fluor 594 Donkey Anti-Guinea Pig (706-585-148,
1026 Jackson ImmunoResearch), Alexa Fluor 488 Donkey Anti-Mouse (715-545-151, Jackson
1027 ImmunoResearch) and Alexa Fluor 647 Donkey Anti-Rabbit (711-605-152, Jackson

1028 ImmunoResearch). Cells were rinsed three times with PBS and microfluidic devices were
1029 mounted with 90% glycerol.
1030 Samples were imaged with a LSM 880 confocal microscope with a 63X 1.4 NA
1031 objective. Images were acquired at zoom 2 in z-stacks of 0.5 µm interval. Typically, 6 images
1032 were acquired per device from the synapse chamber near the postsynaptic chamber such
1033 the image contains multiple dendrites. Images were deconvoluted using the Huygens
1034 software (Scientific Volume Imaging, Netherlands).
1035 Cerebral Organoids: Cerebral organoids were fixed in 4% PFA (w/v) for 30 min at 4°C
1036 followed by three washes with PBS 0.1 M. Cerebral organoids were then placed in sucrose
1037 solution (30% w/v) overnight before being embedded in O.C.T (Tissue-Tek). Embedded
1038 tissue was sectioned at 20 µm using a Cryostar NX70 Cryostat (Thermo Scientific) and
1039 mounted slides were stored at −80°C until immunostaining was performed. For
1040 immunostaining, tissue sections were brought to room temperature and then rehydrated
1041 with 3 washes with 0.1 M PBS, each for 5 mins. Slides were then washed once with PBS with
1042 0.2% Triton X-100 for 15 mins. Tissue was blocked using 10% of donkey serum in PBS 0.1 M
1043 for 1 h at room temperature. After blocking, primary antibodies were added to 0.2 % Triton
1044 X-100 and 10% of donkey serum in PBS 0.1 M at appropriate dilutions and incubated
1045 overnight at 4°C. The next day, slides were washed with PBS 0.1 M 3 times for 5 min each
1046 with gentle shaking. Subsequently, slides were incubated with Alexa Fluor®-conjugated
1047 secondary antibodies in 0.2 % Triton X-100 and 10% of donkey serum in PBS 0.1 M for 2 h at
1048 room temperature in the dark. After secondary antibody incubation, slides were washed 3
1049 times with PBS for 5 min with gentle shanking. Nuclei were visualized by incubating the
1050 tissue for 5 min with Hoechst 33258 stain in PBS 0.1 M. Sections were mounted using
1051 aqueous mounting medium (Polysciences). Images were acquired using an LSM 880
1052 Confocal Scanning Microscope in concert with the ZEISS ZEN imaging software housed at the
1053 Imaging Platform of the Pasteur Institute, Lille. Image acquisition was done at 40X for the
1054 various cellular markers in Fig. 1. The antibodies used were MAP2 (188006, Synaptic
1055 Systems) and GFAP (AB5804, Sigma-Aldrich).
1056
1057 *Quantification of Synaptic Connectivity*
1058 Synaptic connectivity was quantified as previously described (Kilinc et al, 2020). Briefly,
1059 images were analyzed with Imaris software (Bitplane, Zürich, Switzerland) by reconstructing

1060 Synaptophysin I and HOMER1 puncta in 3D. The volume and position information of all
1061 puncta were processed using a custom Matlab (MathWorks, Natick, MA) program. This
1062 program assigns each postsynaptic spot to the nearest presynaptic spot (within a distance
1063 threshold of 1 µm) and calculates the number of such assignments for all presynaptic
1064 puncta.
1065
1066 *Immunoblotting*
1067 Samples from the 2D cultures or brain organoids were collected in RIPA buffer
1068 containing protease and phosphatase inhibitors (Complete mini, Roche Applied Science) and
1069 sonicated several times at 60%-70% for 10 seconds prior to use for the immunoblotting
1070 analyses. Protein quantification was performed using the BCA protein assay (ThermoFisher
1071 Scientific). 10 µg of protein from extracts were separated in NuPAGE 4-12% Bis-Tris Gel
1072 1.0mm (NP0321BOX, Thermo Scientific) or 3-8% Tri-Acetate gel (EA03755BOX, Thermo
1073 Scientific) and transferred on to nitrocellulose membranes 0.2µm (#1704158, Bio-Rad).
1074 Next, membranes were incubated in milk (5% in Tris-buffered saline with 0.1% Tween-20
1075 (TBST)) or SuperBlock (37536, ThermoFisher Scientific) to block non-specific binding sites for
1076 1 hour at room temperature, followed by several washes with TBST 0.1% or TNT 1x as
1077 washing buffers. Immunoblottings were carried out with primary antibodies overnight at
1078 4°C under shaking condition. The membranes were washed three times in the washing
1079 buffer, followed by incubation with HRP-conjugated secondary antibodies for 2 hours at
1080 room temperature under shaking condition. The membranes were washed three times in
1081 washing buffer, and the immune reactivity was revealed using the ECL chemiluminescence
1082 system (SuperSignal, ThermoScientific) and imaged using the Amersham Imager 600 (GE Life
1083 Sciences). Optical densities of bands were quantified using the Gel Analyzer plugin in Fiji–
1084 ImageJ. The primary antibodies used for the immunoblots were as follows: BIN1
1085 (ab182562,Abcam), APP C-terminal (A8717, Sigma-Aldrich), Tau (A002401-2, Agilent)
1086 Phospho-Tau(Clone: AT8) (MN1020,ThermoFisher Scientific), CaV1.3 (CACNA1D) (ACC-005,
1087 Alomone), CaV2.1 (CACNA1A) (ACC-001, Alomone), CaV2.2 (CACNA1B) (ACC-002, Alomone),
1088 CaV2.3 (CACNA1E) (ACC-006, Alomone), CaV1.2 (CACNA1C) (AGP-001 and ACC-003,
1089 Alomone), blocking peptide for Anti-CaV1.2 (CACNA1C) (BLP-CC003, Alomone) and β-ACTIN
1090 (A1978, Sigma-Aldrich). Secondary antibodies used for the immunoblots were Mouse-HRP

1091 (115-035-003, Jackson ImmunoResearch), Rabbit-HRP (111-035-003, Jackson
1092 ImmunoResearch), and Guinea pig-HRP (106-035-003, Jackson ImmunoResearch).
1093
1094 *Activity-dependent endosytosis assay*
1095 ASCL1-hiNs (n=9 cultures from each genotype) were subjected to 30 min of
1096 depolarization with 65 mM KCl or a mock treatment. Cells were then collected and pulled
1097 for endosomal fraction purification using the Minute™ Endosome Isolation and Cell
1098 Fractionation Kit (Invent Biotechnologies). Western blot was performed as described above.
1099
1100 *AlphaLISA measurements*
1101 Cell culture media samples for AlphaLISA measurements were collected at the endof
1102 the 3rd and 4th weeks of differentiation of the ASCL1-hiNs. Alpha-LISA kits specific for
1103 human Aβ1–X (AL288C, PerkinElmer) and Aβ1–42 (AL276C, PerkinElmer) were used to
1104 measure the amount of Aβ1–X and Aβ1–42 respectively in culture media. The human Aβ
1105 analyte standard was diluted in the BrainPhys medium. For the assay, 2 µL of cell culture
1106 medium or standard solution was added to an Optiplate-384 microplate (PerkinElmer). 2 µL
1107 of 10X mixture including acceptor beads and biotinylated antibody was then added to the
1108 wells with culture media or standard solution. Following incubation at room temperature
1109 for an hour, 16 µL of 1.25X donor beads was added to respective wells and incubated at
1110 room temperature for 1 hour. Luminescence was measured using an EnVision-Alpha Reader
1111 (PerkinElmer) at 680-nm excitation and 615-nm emission wavelengths.
1112
1113 *Calcium and iGluSnFR Imaging*
1114 Calcium imaging was performed in 2D cultures after 4 weeks (Ascl1-induced). Prior to
1115 imaging, the cells were incubated with Oregon Green™ 488 BAPTA-1 (OGB-1) acetoxymethyl
1116 (AM) (ThermoFisher Scientific) for 1 h. A 2.5 mM stock solution of the calcium-indicator dye
1117 was prepared in Pluronic™ F-127 (20% solution in DMSO) (ThermoFisher Scientific). 1 µL of
1118 the dye solution was added to 400 µL of fresh BrainPhys medium in each well of a 24-well
1119 cell imaging plate. Existing BrainPhys media from the wells of the plate was removed and
1120 kept aside while the calcium-indicator dye was incubated in fresh BrainPhys medium. After
1121 1 h of incubation, the medium which was kept aside was replaced to each well. The 2D

1122 cultures were then ready to be imaged using a Spinning Disk Microscope (Nikon) housed at
1123 the Institut Pasteur de Lille, Lille, France using the MetaMorph imaging software.
1124 For imaging the calcium activity, 1000 images were taken using a 20× long-distance
1125 objective, with 10 ms exposure time and 200 ms intervals. For each well, 5 random fields
1126 were chosen, and the cellular activity was recorded.
1127 Cells transduced with iGluSnFR were directly imaged after 4 or 6 weeks of
1128 differentiation and 500 images were taken with the same imaging parameters. Up to 8 fields
1129 per well were filmed, each field containing at least one fluorescent transduced cell along
1130 with its processes.
1131
1132 *Analyses of Calcium Transients*
1133 All live recordings of neuronal calcium transients were first converted into .avi format
1134 after background subtraction using the FIJI software. Following the conversion, the videos
1135 were subsequently opened using the free software for data analyses of calcium imaging,
1136 CALciumIMagingAnalyzer (CALIMA) made available online by Fer Radstake (Eindhoven
1137 University of Technology, The Netherlands). Each video recording of a field of cells was first
1138 downscaled to 2X in terms of size with a 10X zoom and was checked for the frame average
1139 mode. Moreover, in this first detection stage, pre-set filter parameters were adjusted and
1140 applied to enable the detection of the maximum number of fluorescent cells in each field. In
1141 the analysis tab, detection of the average activity was checked and for pre-processing, a
1142 median of 3 was applied. All cells within the pre-set filter parameters are detected as
1143 regions of interest (ROIs) in the detection stage. Cell activity from all detected ROIs is then
1144 recorded. However, in the subsequent analysis stage, only cells showing spiking frequencies
1145 with a standard deviation of at least 2 or more were taken into consideration. Data in the
1146 form of detection spikes and the correlation (peak) are extracted and exported as .csv files.
1147
1148 *Electrophysiological recordings in 2D cultures and cerebral organoids*
1149 ASCL1-hiNs were cultured in microfluidic devices bound to multi-electrode arrays
1150 (256MEA100/30iR-ITO, Multi-Channel Systems, Germany). Extracellular action potentials
1151 were recorded in 5 different cultures for both genotypes at 2, 3, 4 and 6 weeks of
1152 differentiation using the MEA2100-256-System (Multi-Channel Systems). Before recordings,
1153 MEAs were let stabilize for 5 min on the headstage to reduce artifacts due to medium

1154 movement. Signals were recorded for 1 min, at 40 kHz sampling rate, using Multi Channel
1155 Experimenter 2.16.0 software (Multi-Channel Systems). Electrical activity in cerebral
1156 organoids was recorded using 256-6wellMEA200/30iR-ITO (Multi-Channel Systems,
1157 Germany). Briefly, 5-6-month-old cerebral organoids were mounted onto MEAs and kept for
1158 2 h in complete Brainphys medium. Then, MEAs were placed on the headstage and let
1159 stabilize for 5 min before recordings. Signals were recorded for 5 min, at 10 kHz sampling
1160 rate using Multi-Channel Experimenter 2.16.0. For rescue experiments using a calcium
1161 channel blocker, ASCL1-hiNs were cultured on MEA 96-well plates (CytoView MEA 96, Axion
1162 Biosystems, USA). Extracellular action potentials were recorded in 3 independent cultures
1163 for either genotype in the presence of 50nM nifedipine (Tocris Bioscience) or vehicle using
1164 the MaestroPro (Axion Biosystems, Inc, USA). Before recordings, MEAs were let stabilize for
1165 5 min on the MaestroPro at 37°C and 5% CO_2. Signals were recorded for 3 min, at 12.5 kHz
1166 sampling rate, using AxIS Navigator software (Axion Biosystems).
1167 Spikes were detected using a fixed amplitude threshold of 5.5 and 4.5 standard
1168 deviations (for the 2D and 3D cultures, respectively) of the high-pass filtered (>300 Hz)
1169 signal for positive- and negative-going signals. The detection included a dead time of 3 ms to
1170 account for the refractory period of action potentials. Quantification of the number of
1171 detected spikes (MUAs) and spike bursts (defined as at least 5 spikes within 50 ms) was
1172 performed using Multi-Channel Analyzer 2.16.0 software (Multi-Channel Systems).
1173
1174 *Spike sorting and temporal structure of spontaneous activity*
1175 Channels containing detected waveforms were manually processed offline for spike
1176 waveform separation and classification using Offline Sorter v3 (Plexon, USA). Briefly, we
1177 applied principal component analysis (PCA) to cluster spike waveforms of similar
1178 morphologies. Using this approach, we identified from 2 to 10 well-isolated units per
1179 channel, and therefore, we considered this single-unit activity (SUA). For each SUA, we
1180 computed the average firing rate, the signal-to-noise ratio, the peak-to-trough amplitude
1181 and duration, the average power (square amplitude of the average waveform), the mode of
1182 the interspike interval distribution, and their firing patterns. It has been demonstrated that
1183 dissociated neuronal cultures can develop complex discharge structures [47]. Here, we
1184 considered burst activity if the SUA presents periods of high-frequency discharges
1185 interspersed by regular or no discharges at all. Operationally, a burst must have at least 3

1186 spikes within 100 ms and 200 ms intervals, for the interval between the first and the second,
1187 and the second and the third discharge, respectively. After the third spike, the maximal
1188 interval to consider a discharge part of the burst was 200 ms. Thus, we computed the SUA
1189 that presented bursts, the number of bursts (i.e., the burst frequency), the average burst
1190 duration, the number of spikes within each burst, the average burst frequency, and the
1191 inter-burst interval. To evaluate the temporal structures of spike trains, we computed the
1192 array-wide spike detection rate (ASDR), which is the number of spikes detected per unit of
1193 time, summed over all electrodes in the array. This method is commonly used in the
1194 literature to demonstrate synchronous activity (aka, bursts) in MUA data (Wagenaar, 2006).
1195
1196 *snRNA-seq Library Preparation*
1197 Nuclei isolation and Hash-tagging with oligonucleotides steps were realized on ice with
1198 pre-cold buffers and centrifugations at 4°C. 6.5-month-old BIN1 WT, HET, and KO organoids
1199 were processed as previously (Lambert et al., 2022). 4-week-old cultured ASCL1-induced
1200 BIN1 WT and KO 2D cultures were washed in the imaging plate wells with 500 µL of
1201 Deionized Phosphate Buffer Saline 1X (DPBS, GIBCO™, Fisher Scientific 11590476). Cells
1202 were resuspended with wide bore tips in 500 µL Lysis Buffer (Tris-HCL 10mM, NaCl 10mM,
1203 MgCl2 3mM, Tween-20 0,1%, Nonidet P40 Substitute 0,1%, Digitonin 0,01%, BSA 1%,
1204 Invitrogen™ RNAseout™ recombinant ribonuclease inhibitor 0,04 U/µL). Multiple
1205 mechanical resuspensions in this buffer were performed for a total lysis time of 15 mins.,
1206 500 µL of washing buffer was added (Tris-HCL 10mM, NaCl 10 mM, MgCl2 3 mM, Tween-20
1207 0.1%, BSA 1%, Invitrogen™ RNAseout™ recombinant ribonuclease inhibitor 0,04 U/µL) and
1208 the lysis suspension was centrifuged 8 mins. at 500 g (used for all following centrifugation
1209 steps). Nuclei pellets were washed tree times with one filtration step by MACS pre-
1210 separation filter 20µm (Miltenyi Biotec). Nuclei pellets were resuspended in 100 µL of
1211 staining buffer (DPBS BSA 2%, Tween-20 0.01%), 10 µL of Fc blocking reagent
1212 HumanTruStainFc™ (422302, Biolegend) and incubated 5 min at 4°C. 1µl of antibody was
1213 added (Total-Seq™-A0453 anti-Vertebrate Nuclear Hashtag 3 MAb414 for the WT and Total-
1214 Seq™-A0454 anti-Vertebrate Nuclear Hashtag 4 MAb414 for the KO, 97286 and 97287
1215 respectively, Biolegend) and incubated 15 mins. at 4°C. Nuclei pellets were washed three
1216 times in staining buffer with one filtration step by MACS pre-separation filter 20 µm
1217 (Miltenyi Biotec) to a final resuspension in 300 µL of staining buffer for Malassez cell

1218 counting with Trypan blue counterstaining (Trypan Blue solution, 11538886,
1219 Fisherscientific). Isolated nuclei were loaded on a Chromium 10X genomics controller
1220 following the manufacturer protocol using the chromium single-cell v3 chemistry and single
1221 indexing and the adapted protocol by Biolegend for the HTO library preparation. The
1222 resulting libraries were pooled at equimolar proportions with a 9 for 1 ratio for Gene
1223 expression library and HTO library respectively. Finally, the pool was sequenced using 100pb
1224 paired-end reads on NOVAseq 6000 system following the manufacturer recommendations
1225 (Illumina).
1226
1227 *snRNA-seq Dataset Preprocessing*
1228 Unique Molecular Index (UMI) Count Matrices for gene expression and for Hash Tag
1229 Oligonucleotide (HTO) libraries were generated using the CellRanger count (Feature
1230 Barcode) pipeline. Reads were aligned on the GRCh38-3.0.0 transcriptome reference (10x
1231 Genomics). Filtering for low quality cells according to the number of RNA, genes detected,
1232 and percentage of mitochondrial RNA was performed. For HTO sample, the HTO matrix was
1233 normalized using centered log-ratio (CLR) transformation and cells were assigned back to
1234 their sample of origin using HTODemux function of the Seurat R Package (v4) [48]. Then,
1235 normalizations of the gene expression matrix for cellular sequencing depth, mitochondrial
1236 percentage and cell cycle phases using the variance stabilizing transformation (vst) based
1237 Seurat:SCTransform function were performed.
1238
1239 *snRNA-seq datasets integration and annotation*
1240 To integrate the datasets from independent experiments, the harmony R package
1241 (https://github.com/immunogenomics/harmony) was used. In order to integrate the
1242 datasets, the SCTransform normalized matrices was merged and PCA was performed using
1243 Seurat::RunPCA default parameter. The 50 principal components (dimensions) of the PCA
1244 were corrected for batch effect using harmony::RunHarmony function. Then, the 30 first
1245 batch corrected dimensions were used as input for graph-based cell clustering and
1246 visualization tool. Seurat::FindNeighbors using default parameters and Seurat::FindClusters
1247 function using the Louvain algorithm were used to cluster cells according to their batch
1248 corrected transcriptomes similarities. To visualize the cells similarities in a 2-dimension

1249 space, the Seurat::RunUMAP function using default parameter was used. Cell clusters were
1250 then annotated based on cell type specific gene expression markers.
1251
1252 *Differential gene expression and GO enrichment analyses*
1253 For snRNA-seq experiment reproduce 2 times or less (*i.e.* organoid and nifedipine
1254 experiments), gene expression within each main cell type was compared between
1255 conditions of interest using Wilcoxon test on the SCTransform normalized gene expression
1256 matrix. For snRNA-seq experiment reproduce more than 2 times (*BIN1* KO vs WT hiNs
1257 comparison), Pseudobulk differential expression analysis was performed using the package
1258 DESeq2 (CRAN). For each main cell type, the cell level gene expression matrix was first
1259 aggregate at the sample level using Matrix:: aggregate.Matrix function. Genes detected in
1260 more than 100 cells or in 10% of the cells was test for differential expression using DESeq
1261 function, including in the model the experiment batch as covariate.
1262 GO enrichment analysis on the differentially expressed genes was performed using
1263 the gost function of the gprofiler2 R package (CRAN), using default parameter, or, if
1264 specified using fast gene-set enrichement analysis (FGSEA, [49]) package (Bioconductor).
1265
1266 *Activity-related genes (ARGs) signature enrichment analysis at single cell resolution*
1267 To study enrichment for activity-related genes (ARGs) signature across cerebral
1268 organoid cells, the CellID R package (https://github.com/RausellLab/CelliD) was used. ARGs
1269 obtained from Tyssowski et al. (2018) and Hravtin et al. (2018) (supplementary Table 7),
1270 were translated to the corresponding human gene name with the help of the biomaRt
1271 package using the respective Ensembl references. Then, the CellID::RunMCA was used to
1272 extract cell-specific gene signature and hypergeometric test was performed to test
1273 enrichment for ARGs in these cell signatures. To test the differential proportion of ARGs
1274 enriched cells in BIN1 deleted organoid compared to WT organoid, chi-squared test was
1275 performed.
1276
1277 *Comparative analysis with specific DEGs in AD brains*
1278 To compare the transcriptomic change observed in BIN1 deleted cerebral organoid
1279 with those observed in AD brain we used the dataset available for download at Synapse.org
1280 under the Synapse ID syn21788402 [35]. The raw gene expression matrix was normalized

1281 using Seurat::SCTransform and differential expression analysis was performed within each
1282 neuronal cell type using Wilcoxon test as used for our organoid dataset. AD related DEGs,
1283 thus, obtained were compared with our BIN1 related organoid DEGs in every cell type. To
1284 this end, the enrichment for AD-related DEGs in BIN1-related DEGs was tested using
1285 hypergeometric test. The background for this test was defined as all genes detected in both
1286 datasets. The p-value of this test was used as metrics to compare the significance of the
1287 gene overlap between neuronal cell types.
1288
1289 *Statistical analyses*
1290 Statistical analyses were performed using GraphPad Prism version 8.0.0 (GraphPad
1291 Software, San Diego, California USA, www.graphpad.com) and R 4.2.0 (R Core Team, 2022,
1292 https://cran.r-project.org/bin/windows/base/old/4.2.0/). Bar plots show mean ± SD and
1293 individual values. Box plots show 1-99 percentile. Statistical tests and p values are indicated
1294 in figure legends.
1295

Figure 1

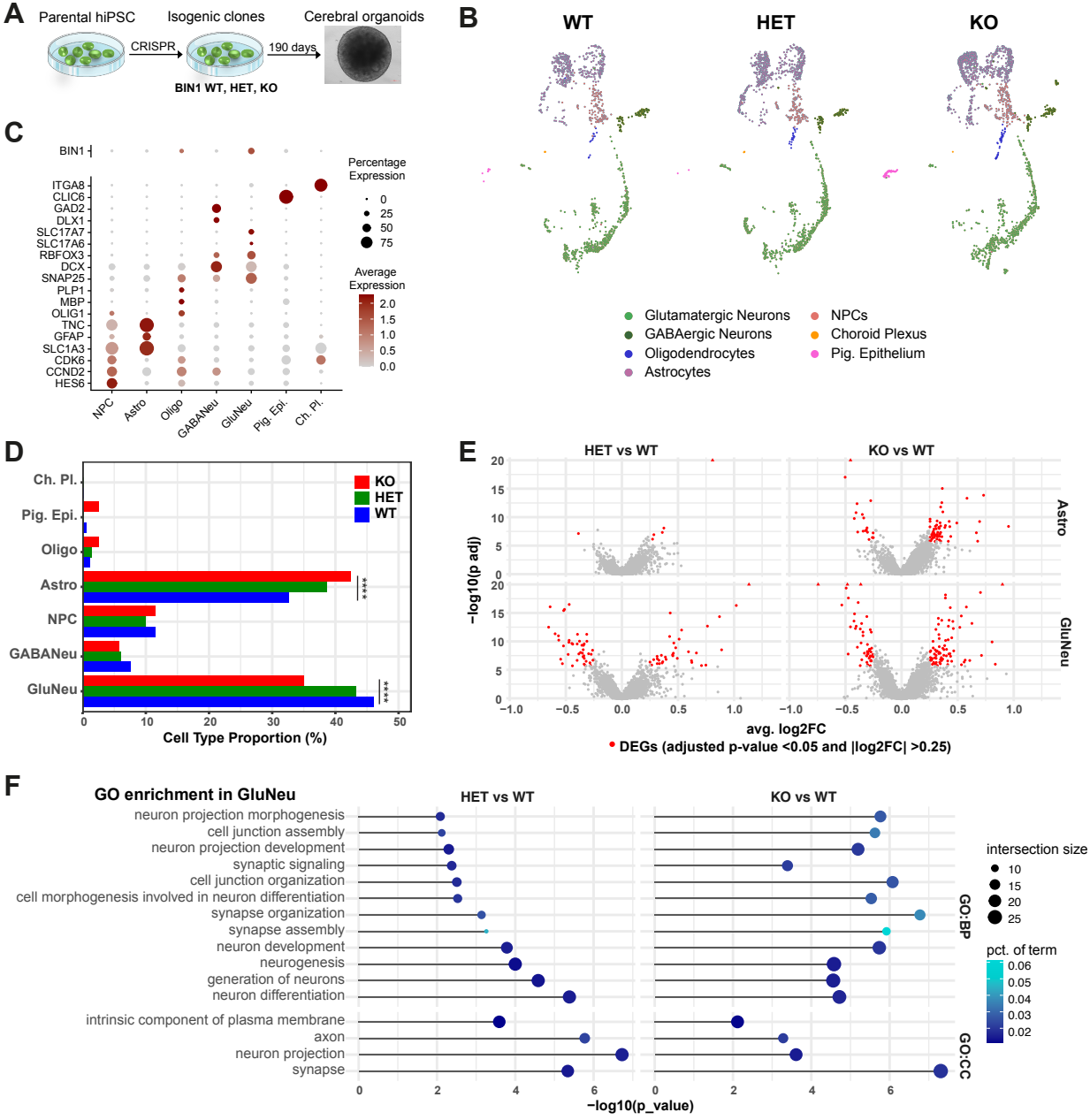
A
Parental hiPSC
Isogenic clones
Cerebral organoids
CRISPR
190 days
BIN1 WT, HET, KO
B
WT
HET
KO
Glutamatergic Neurons
GABAergic Neurons
Oligodendrocytes
Astrocytes
NPCs
Choroid Plexus
Pig. Epithelium
C
BIN1
ITGA8
CLIC6
GAD2
DLX1
SLC17A7
SLC17A6
RBFOX3
DCX
SNAP25
PLP1
MBP
OLIG1
TNC
GFAP
SLC1A3
CDK6
CCND2
HES6
NPC
Astro
Oligo
GABANeu
GluNeu
Pig. Epi.
Ch. Pl.
Percentage Expression
0
25
50
75
Average Expression
2.0
1.5
1.0
0.5
0.0
D
Ch. Pl.
Pig. Epi.
Oligo
Astro
NPC
GABANeu
GluNeu
KO
HET
WT
****
****
0
10
20
30
40
50
Cell Type Proportion (%)
E
HET vs WT
KO vs WT
Astro
GluNeu
−log10(p adj)
avg. log2FC
DEGs (adjusted p-value <0.05 and |log2FC| >0.25)
F
GO enrichment in GluNeu
HET vs WT
KO vs WT
neuron projection morphogenesis
cell junction assembly
neuron projection development
synaptic signaling
cell junction organization
cell morphogenesis involved in neuron differentiation
synapse organization
synapse assembly
neuron development
neurogenesis
generation of neurons
neuron differentiation
intrinsic component of plasma membrane
axon
neuron projection
synapse
GO:BP
GO:CC
intersection size
10
15
20
25
pct. of term
0.06
0.05
0.04
0.03
0.02
−log10(p_value)

Figure 2

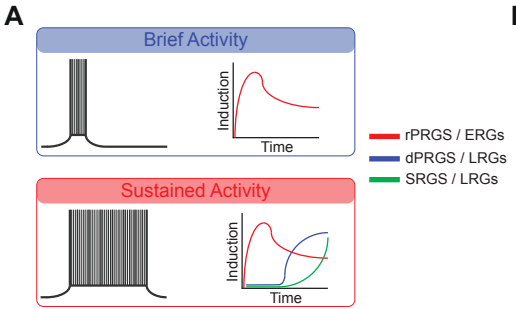
A
Brief Activity
Induction
Time
Sustained Activity
Induction
Time
rPRGS / ERGs
dPRGS / LRGs
SRGS / LRGs

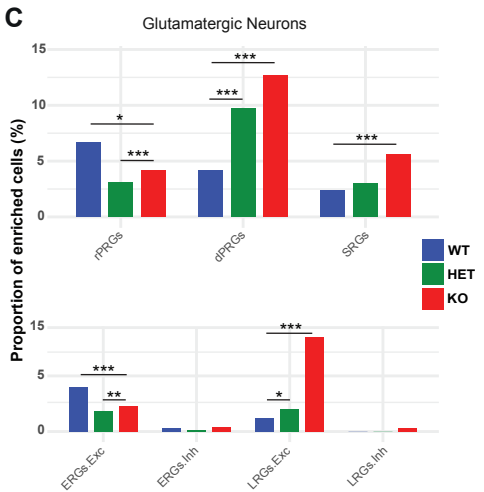
C
Glutamatergic Neurons
Proportion of enriched cells (%)
15
10
5
0
*
***
***
***
***
rPRGs
dPRGs
SRGs
WT
HET
KO
15
5
0
***
**
***
*
ERGs.Exc
ERGs.Inh
LRGs.Exc
LRGs.Inh

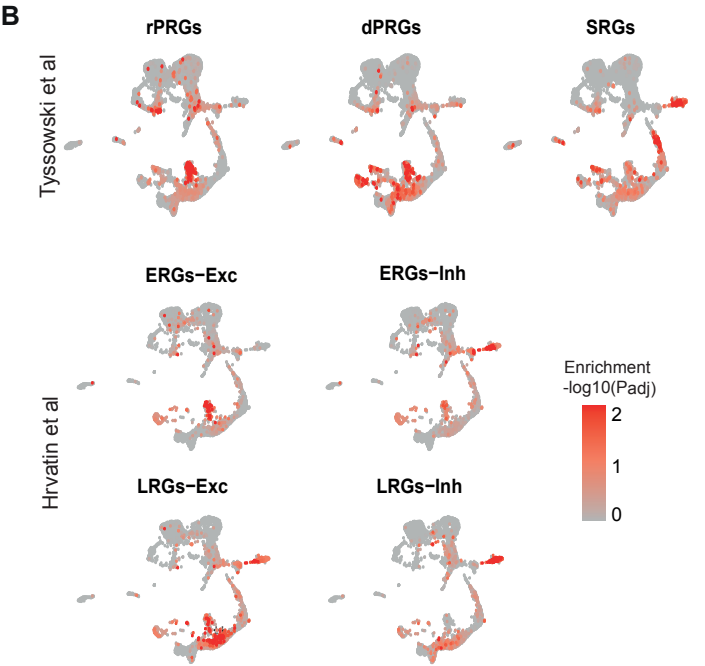
B
rPRGs
dPRGs
SRGs
Tyssowski et al
ERGs−Exc
ERGs−Inh
LRGs−Exc
LRGs−Inh
Hrvatin et al
Enrichment
-log10(Padj)
2
1
0

Figure 3

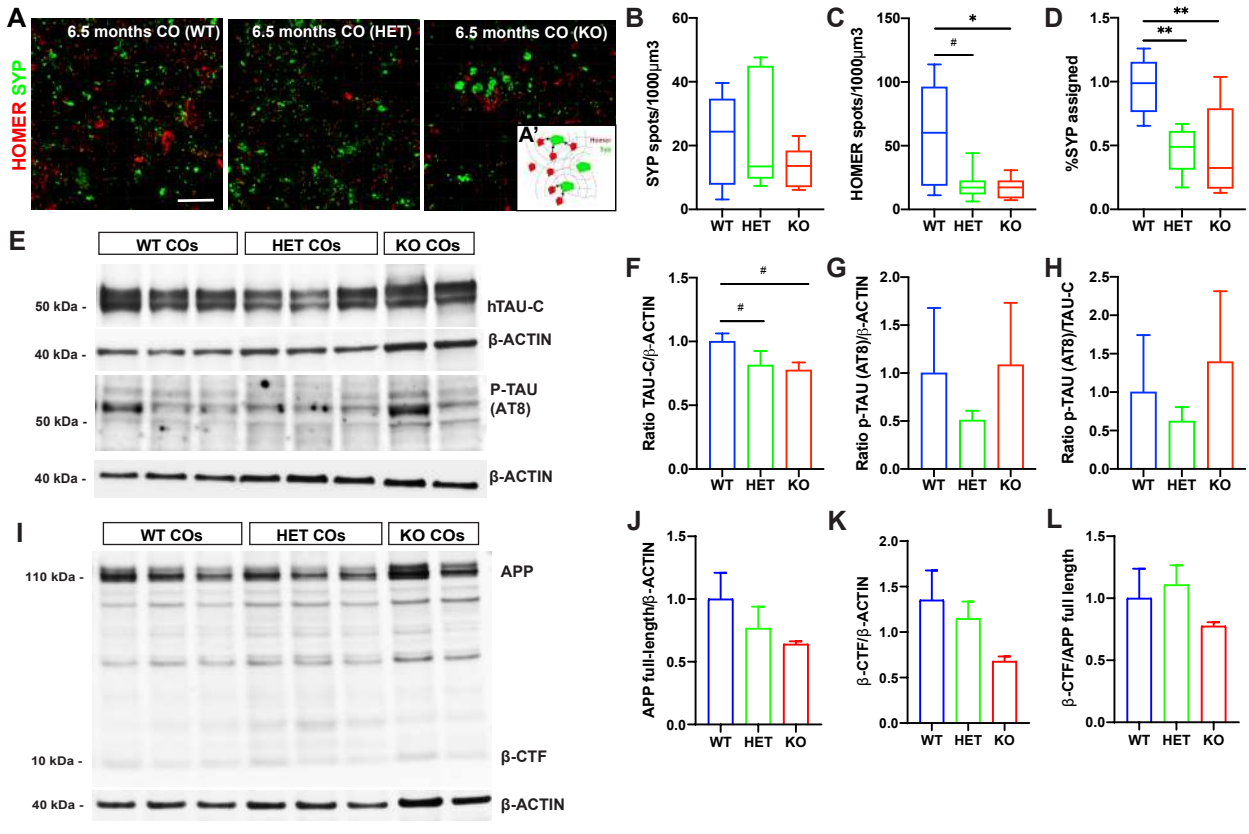
A
6.5 months CO (WT)
6.5 months CO (HET)
6.5 months CO (KO)
HOMER SYP
A'
B
SYP spots/1000µm3
C
HOMER spots/1000µm3
D
%SYP assigned
WT HET KO
E
WT COs
HET COs
KO COs
50 kDa -
40 kDa -
hTAU-C
β-ACTIN
P-TAU (AT8)
F
Ratio TAU-C/β-ACTIN
G
Ratio p-TAU (AT8)/β-ACTIN
H
Ratio p-TAU (AT8)/TAU-C
I
110 kDa -
10 kDa -
APP
β-CTF
J
APP full-length/β-ACTIN
K
β-CTF/β-ACTIN
L
β-CTF/APP full length

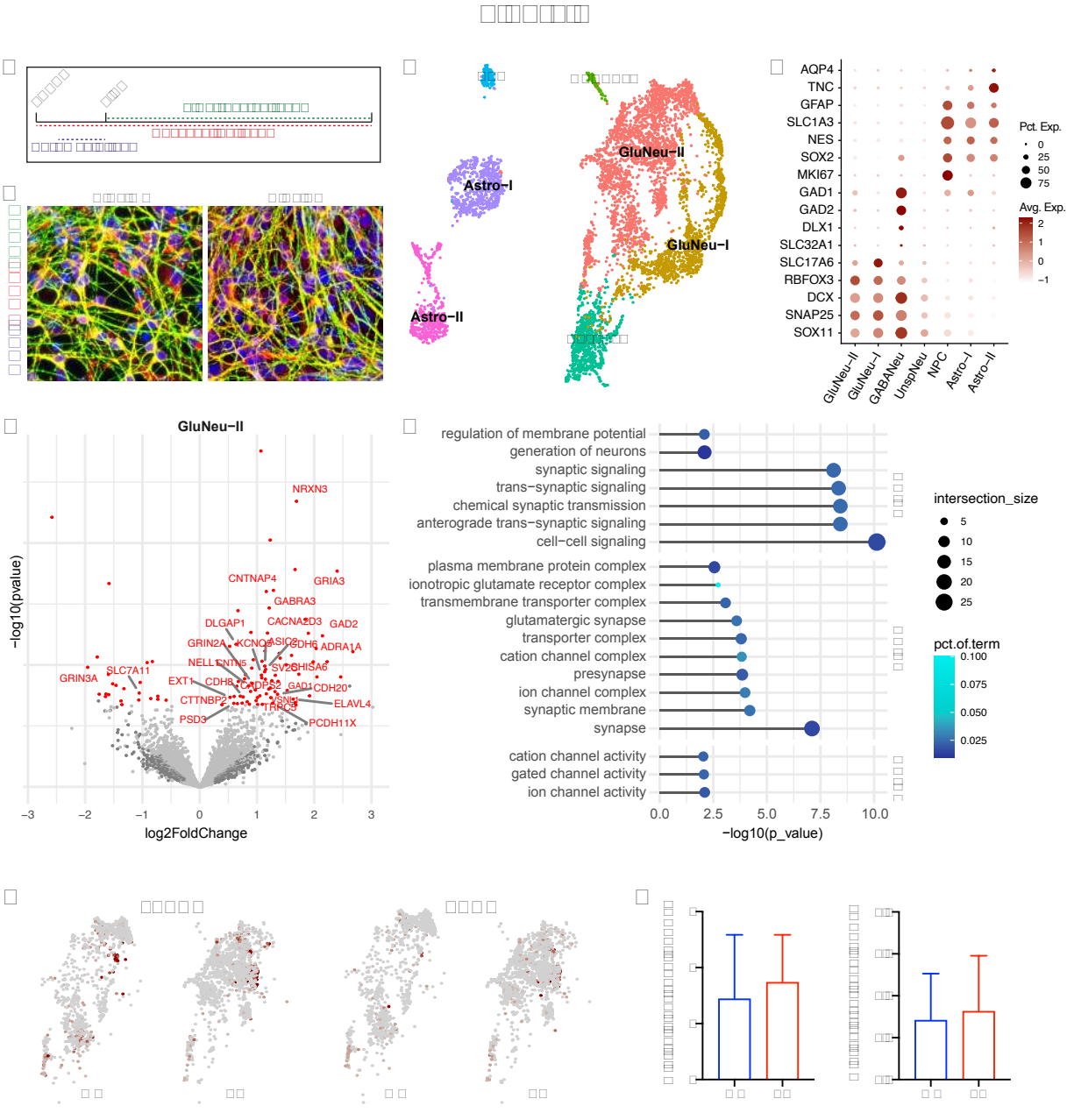

GluNeu−II
Astro−I
Astro−II
GluNeu−I
AQP4
TNC
GFAP
SLC1A3
NES
SOX2
MKI67
GAD1
GAD2
DLX1
SLC32A1
SLC17A6
RBFOX3
DCX
SNAP25
SOX11
GluNeu−II
GluNeu−I
GABANeu
UnspNeu
NPC
Astro−I
Astro−II
Pct. Exp.
0
25
50
75
Avg. Exp.
2
1
0
−1
GluNeu−II
NRXN3
CNTNAP4
GRIA3
GABRA3
DLGAP1
CACNA2D3
GAD2
GRIN2A
KCNQ5
ASIC2
CDH6
ADRA1A
NELL1
CNTN5
SV2C
HISA6
GRIN3A
SLC7A11
EXT1
CDH8
CADPS2
GAD1
CDH20
CTTNBP2
VSNL1
ELAVL4
TRPC3
PSD3
PCDH11X
−log10(pvalue)
log2FoldChange
−3
−2
−1
0
1
2
3
regulation of membrane potential
generation of neurons
synaptic signaling
trans−synaptic signaling
chemical synaptic transmission
anterograde trans−synaptic signaling
cell−cell signaling
plasma membrane protein complex
ionotropic glutamate receptor complex
transmembrane transporter complex
glutamatergic synapse
transporter complex
cation channel complex
presynapse
ion channel complex
synaptic membrane
synapse
cation channel activity
gated channel activity
ion channel activity
0.0
2.5
5.0
7.5
10.0
−log10(p_value)
intersection_size
5
10
15
20
25
pct.of.term
0.100
0.075
0.050
0.025

Figure 5

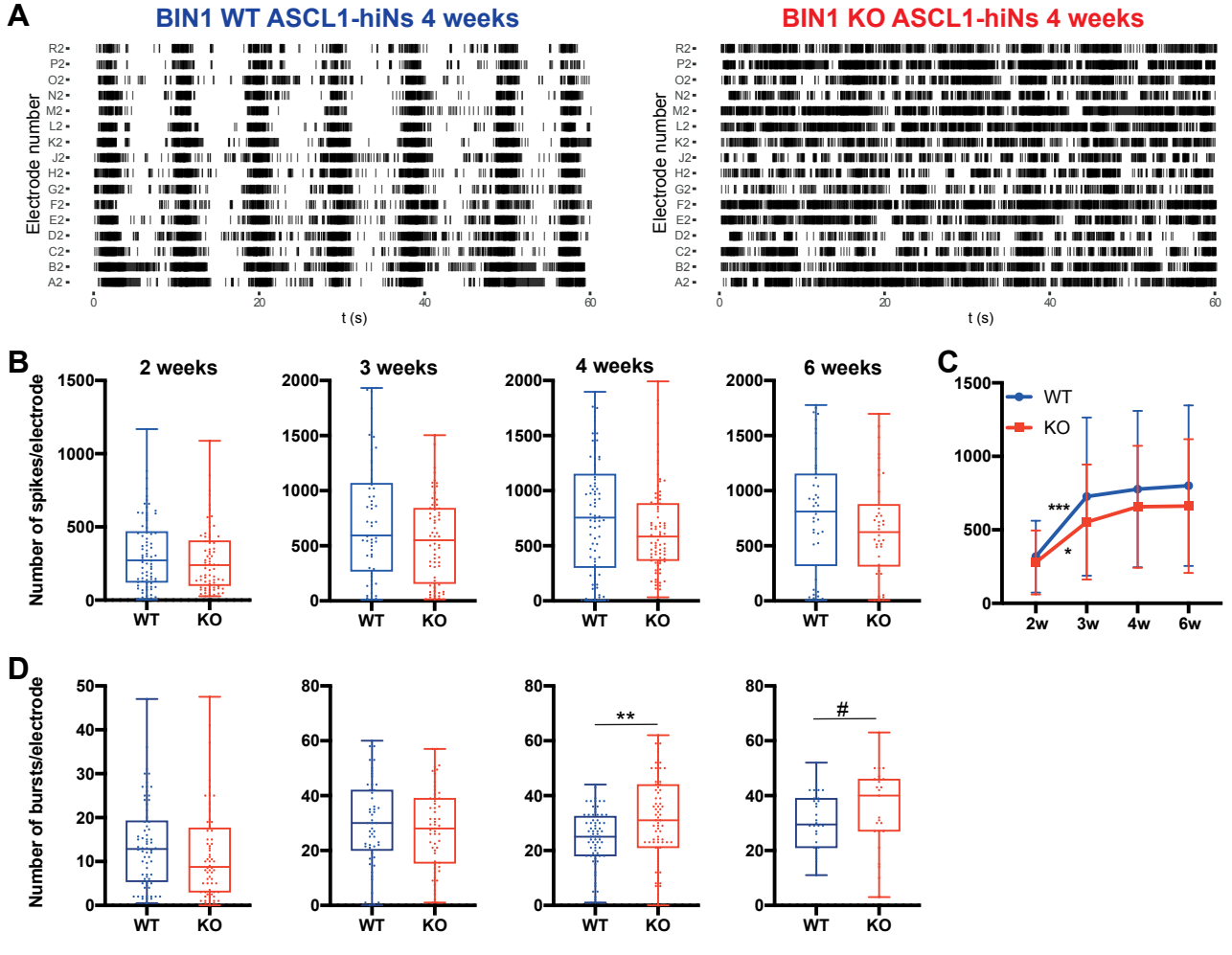
A
BIN1 WT ASCL1-hiNs 4 weeks
BIN1 KO ASCL1-hiNs 4 weeks
Electrode number
R2
P2
O2
N2
M2
L2
K2
J2
H2
G2
F2
E2
D2
C2
B2
A2
0
20
40
60
t (s)
B
2 weeks
3 weeks
4 weeks
6 weeks
Number of spikes/electrode
WT
KO
C
WT
KO
***
*
2w
3w
4w
6w
D
Number of bursts/electrode
**
#

Figure 6

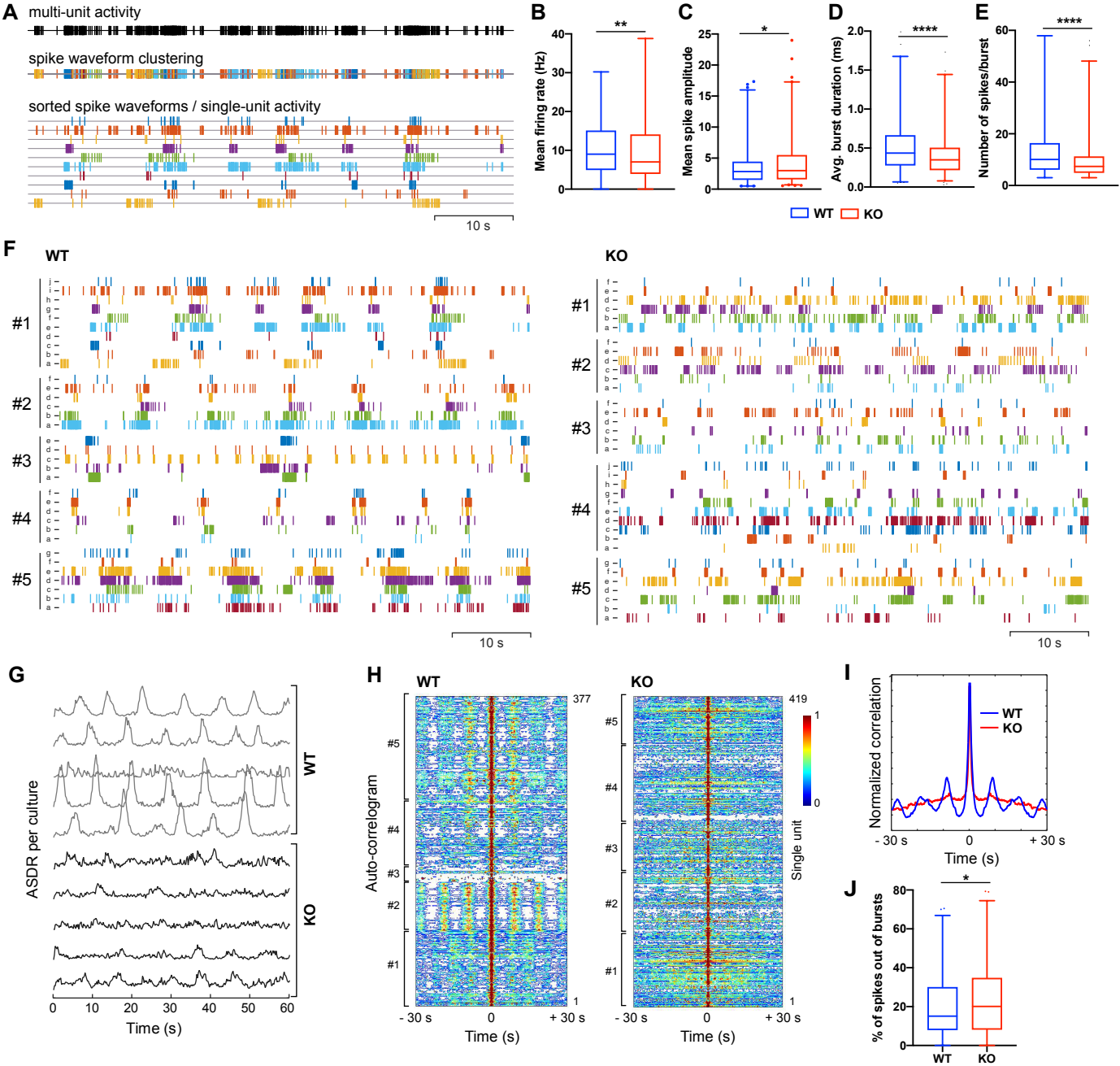
A
multi-unit activity
spike waveform clustering
sorted spike waveforms / single-unit activity
10 s
B
Mean firing rate (Hz)
**
C
Mean spike amplitude
*
D
Avg. burst duration (ms)
****
E
Number of spikes/burst
****
WT
KO
F
WT
KO
#1
#2
#3
#4
#5
10 s
G
ASDR per culture
WT
KO
Time (s)
H
WT
KO
Auto-correlogram
Single unit
377
419
1
0
- 30 s
0
+ 30 s
Time (s)
I
Normalized correlation
WT
KO
- 30 s
0
+ 30 s
Time (s)
J
% of spikes out of bursts
*
WT
KO

Figure 7

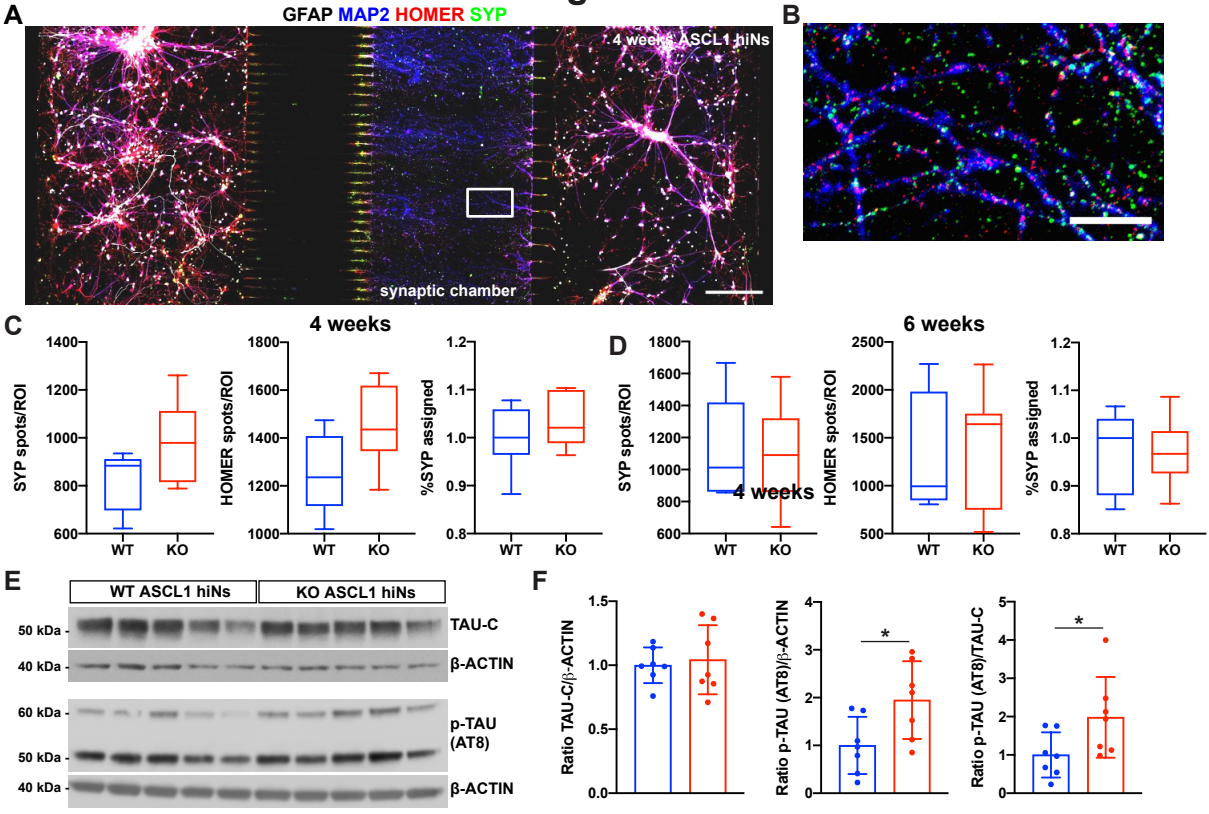
A
GFAP MAP2 HOMER SYP
4 weeks ASCL1 hiNs
synaptic chamber
B
C
4 weeks
SYP spots/ROI
HOMER spots/ROI
%SYP assigned
WT
KO
D
6 weeks
4 weeks
E
WT ASCL1 hiNs
KO ASCL1 hiNs
50 kDa
40 kDa
TAU-C
β-ACTIN
60 kDa
p-TAU (AT8)
F
Ratio TAU-C/β-ACTIN
Ratio p-TAU (AT8)/β-ACTIN
Ratio p-TAU (AT8)/TAU-C
*

Figure 8

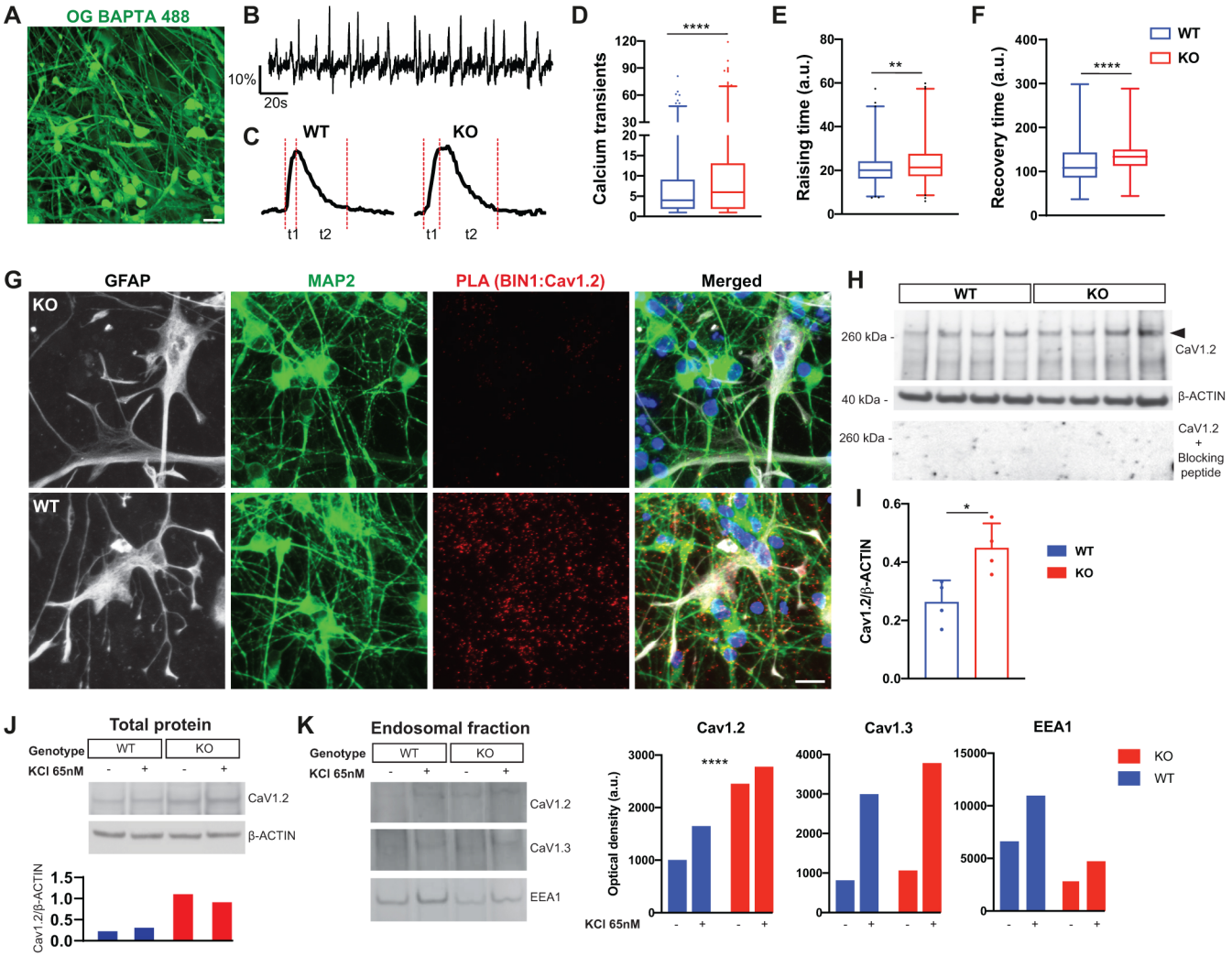
A
OG BAPTA 488
B
10%
20s
C
WT
KO
t1
t2
D
Calcium transients
****
E
Raising time (a.u.)
**
F
Recovery time (a.u.)
****
WT
KO
G
GFAP
MAP2
PLA (BIN1:Cav1.2)
Merged
KO
WT
H
WT
KO
260 kDa -
CaV1.2
40 kDa -
β-ACTIN
260 kDa -
CaV1.2 + Blocking peptide
I
Cav1.2/β-ACTIN
*
WT
KO
J
Total protein
Genotype
WT
KO
KCl 65nM
CaV1.2
β-ACTIN
Cav1.2/β-ACTIN
K
Endosomal fraction
Genotype
WT
KO
KCl 65nM
CaV1.2
CaV1.3
EEA1
Cav1.2
Cav1.3
EEA1
Optical density (a.u.)
****
KO
WT

Figure 9

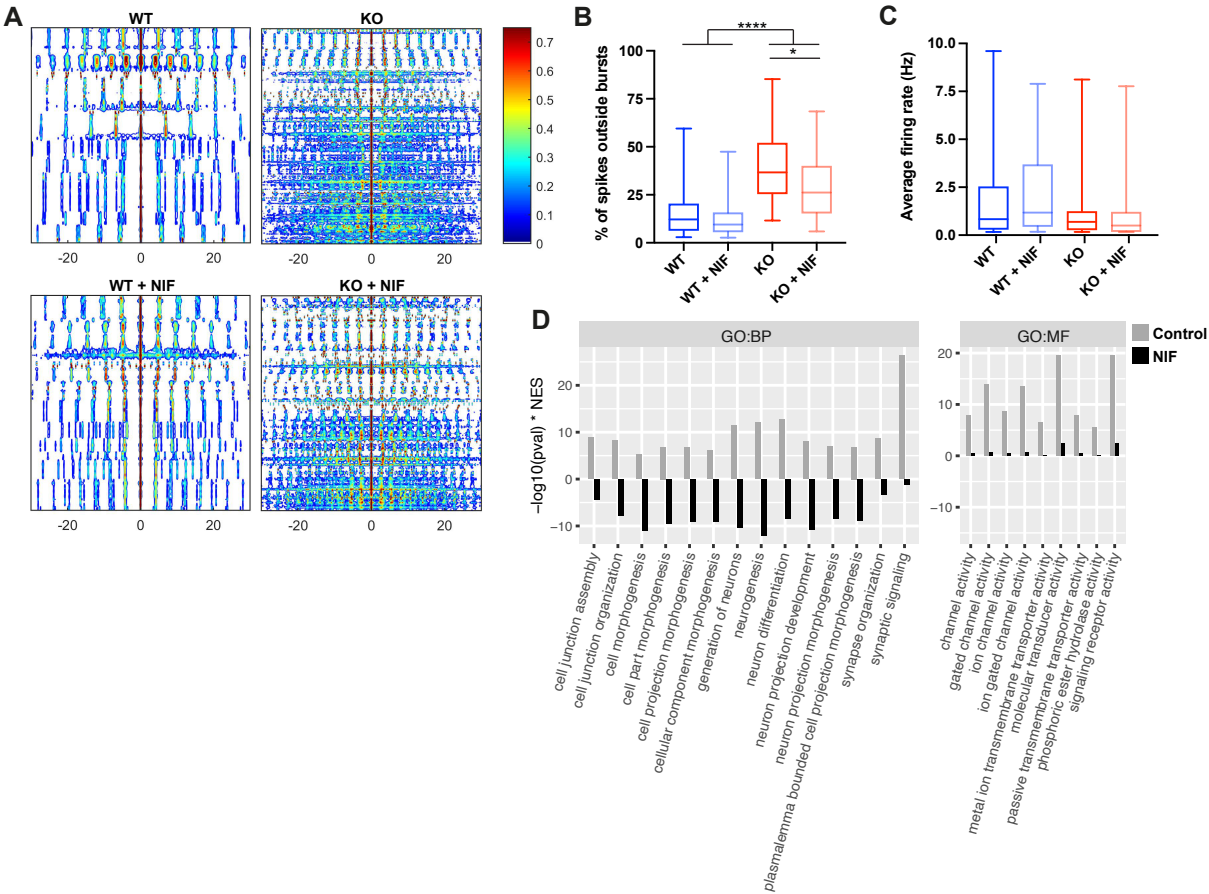
A
WT
KO
WT + NIF
KO + NIF
-20
0
20
0.7
0.6
0.5
0.4
0.3
0.2
0.1
0
B
% of spikes outside bursts
100
75
50
25
0
****
*
WT
WT + NIF
KO
KO + NIF
C
Average firing rate (Hz)
10.0
7.5
5.0
2.5
0.0
WT
WT + NIF
KO
KO + NIF
D
GO:BP
GO:MF
Control
NIF
−log10(pval) * NES
20
10
0
−10
cell junction assembly
cell junction organization
cell morphogenesis
cell part morphogenesis
cell projection morphogenesis
cellular component morphogenesis
generation of neurons
neurogenesis
neuron differentiation
neuron projection development
neuron projection morphogenesis
plasmalemma bounded cell projection morphogenesis
synapse organization
synaptic signaling
channel activity
gated channel activity
ion channel activity
ion gated channel activity
metal ion transmembrane transporter activity
molecular transducer activity
passive transmembrane transporter activity
phosphoric ester hydrolase activity
signaling receptor activity

Figure 10

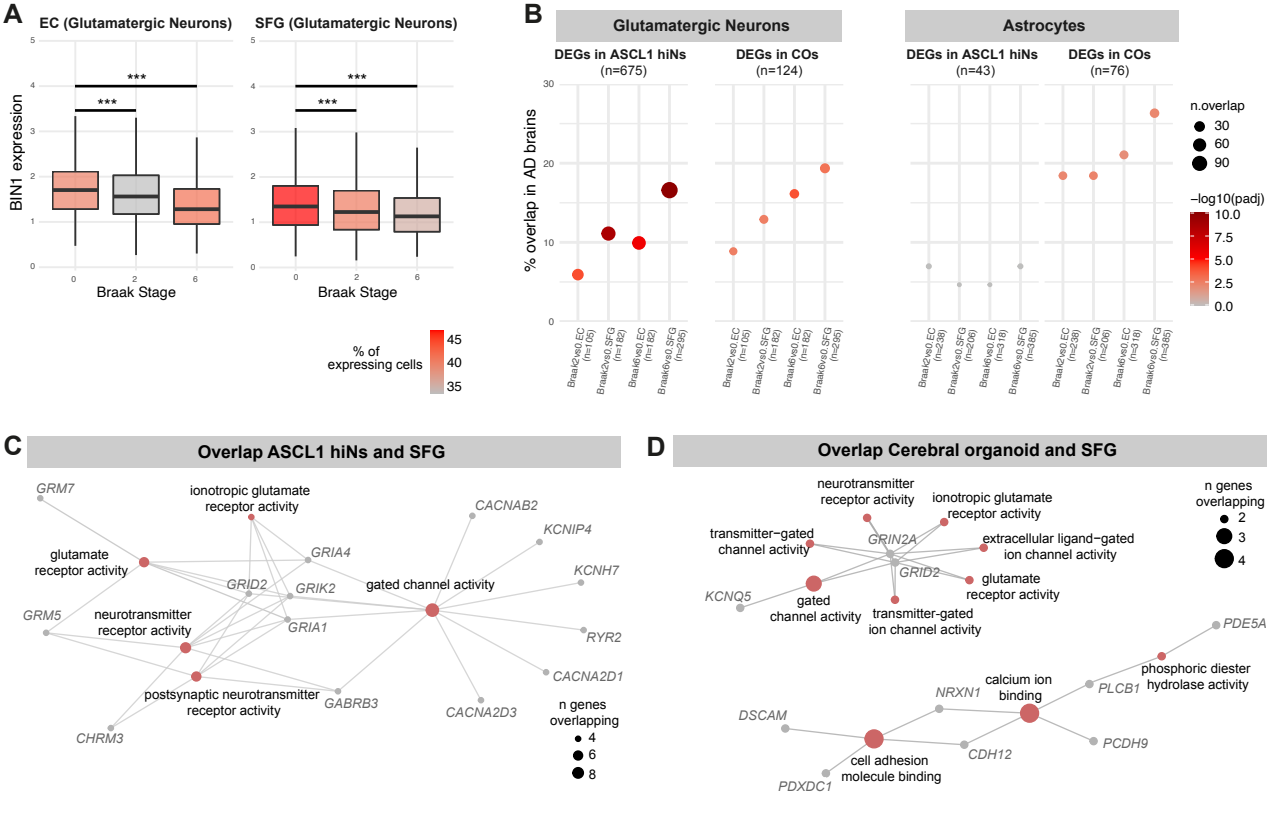
A
EC (Glutamatergic Neurons)
SFG (Glutamatergic Neurons)
BIN1 expression
Braak Stage
***
% of expressing cells
45
40
35
B
Glutamatergic Neurons
Astrocytes
DEGs in ASCL1 hiNs (n=675)
DEGs in COs (n=124)
DEGs in ASCL1 hiNs (n=43)
DEGs in COs (n=76)
% overlap in AD brains
n.overlap
30
60
90
−log10(padj)
10.0
7.5
5.0
2.5
0.0
C
Overlap ASCL1 hiNs and SFG
GRM7
ionotropic glutamate receptor activity
CACNAB2
KCNIP4
glutamate receptor activity
GRIA4
GRID2
GRIK2
gated channel activity
KCNH7
GRM5
neurotransmitter receptor activity
GRIA1
RYR2
CACNA2D1
postsynaptic neurotransmitter receptor activity
GABRB3
CACNA2D3
CHRM3
n genes overlapping
4
6
8
D
Overlap Cerebral organoid and SFG
neurotransmitter receptor activity
ionotropic glutamate receptor activity
transmitter−gated channel activity
GRIN2A
extracellular ligand−gated ion channel activity
GRID2
glutamate receptor activity
KCNQ5
gated channel activity
transmitter-gated ion channel activity
n genes overlapping
2
3
4
PDE5A
phosphoric diester hydrolase activity
PLCB1
NRXN1
calcium ion binding
DSCAM
PCDH9
CDH12
cell adhesion molecule binding
PDXDC1

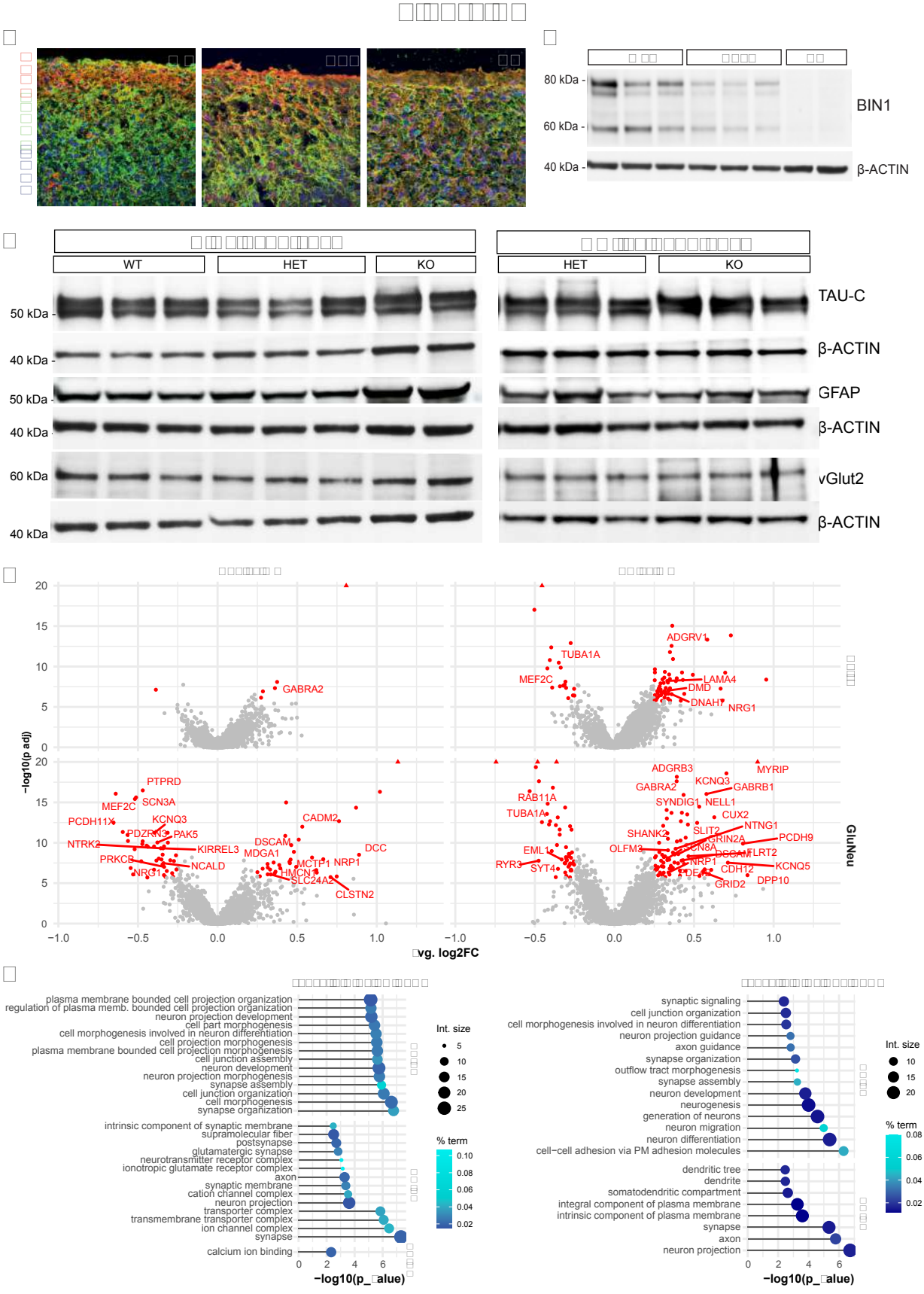

80 kDa
60 kDa
40 kDa
BIN1
β-ACTIN
WT
HET
KO
HET
KO
50 kDa
40 kDa
50 kDa
40 kDa
60 kDa
40 kDa
TAU-C
β-ACTIN
GFAP
β-ACTIN
vGlut2
β-ACTIN
−log10(p adj)
vg. log2FC
GluNeu
GABRA2
TUBA1A
MEF2C
ADGRV1
LAMA4
DMD
DNAH7
NRG1
PTPRD
MEF2C
SCN3A
PCDH11X
KCNQ3
PDZRN3
PAK5
NTRK2
KIRREL3
PRKCB
NCALD
NRG1
CADM2
DSCAM
MDGA1
MCTP1
NRP1
HMCN1
SLC24A2
CLSTN2
DCC
ADGRB3
MYRIP
GABRA2
KCNQ3
GABRB1
RAB11A
SYNDIG1
NELL1
TUBA1A
CUX2
NTNG1
SHANK2
SLIT2
GRIN2A
PCDH9
OLFM3
SCN8A
DSCAM
FLRT2
EML1
NRP1
CDH12
KCNQ5
RYR3
SYT4
PDE4B
GRID2
DPP10
plasma membrane bounded cell projection organization
regulation of plasma memb. bounded cell projection organization
neuron projection development
cell part morphogenesis
cell morphogenesis involved in neuron differentiation
cell projection morphogenesis
plasma membrane bounded cell projection morphogenesis
cell junction assembly
neuron development
neuron projection morphogenesis
synapse assembly
cell junction organization
cell morphogenesis
synapse organization
intrinsic component of synaptic membrane
supramolecular fiber
postsynapse
glutamatergic synapse
neurotransmitter receptor complex
ionotropic glutamate receptor complex
axon
synaptic membrane
cation channel complex
neuron projection
transporter complex
transmembrane transporter complex
ion channel complex
synapse
calcium ion binding
Int. size
% term
−log10(p_alue)
synaptic signaling
cell junction organization
cell morphogenesis involved in neuron differentiation
neuron projection guidance
axon guidance
synapse organization
outflow tract morphogenesis
synapse assembly
neuron development
neurogenesis
generation of neurons
neuron migration
neuron differentiation
cell−cell adhesion via PM adhesion molecules
dendritic tree
dendrite
somatodendritic compartment
integral component of plasma membrane
intrinsic component of plasma membrane
synapse
axon
neuron projection
Int. size
% term
−log10(p_alue)

Figure S2

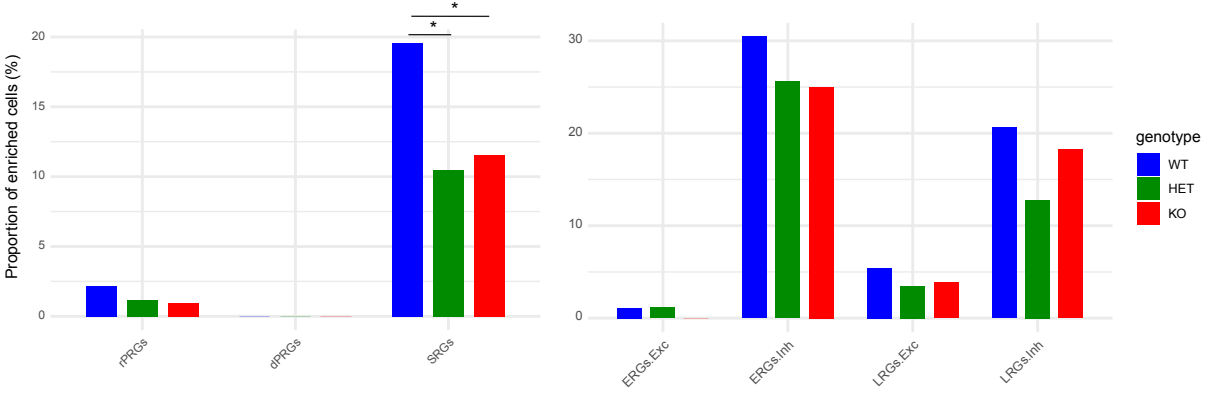
Proportion of enriched cells (%)
20
15
10
5
0
*
*
rPRGs
dPRGs
SRGs
30
20
10
0
ERGs.Exc
ERGs.Inh
LRGs.Exc
LRGs.Inh
genotype
WT
HET
KO

Figure S3

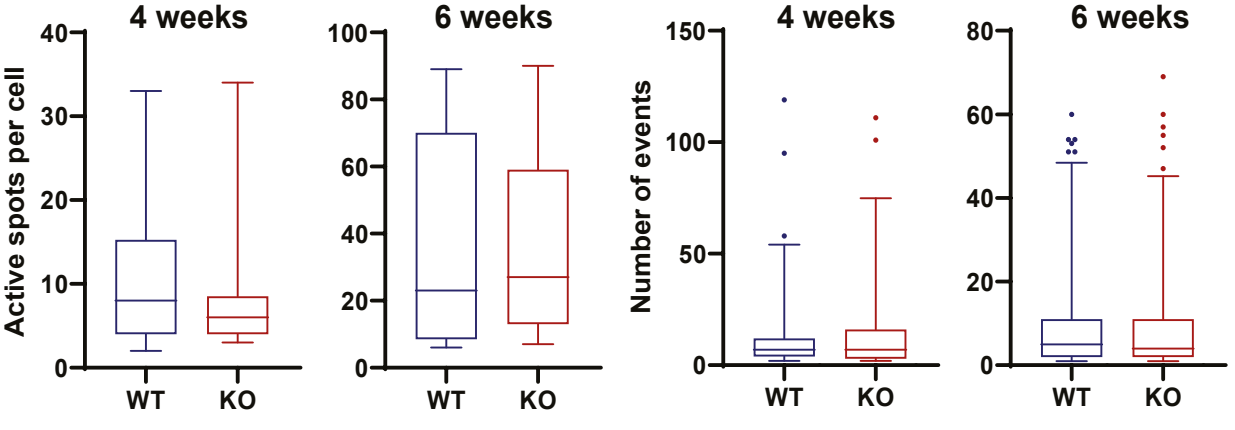
4 weeks
6 weeks
4 weeks
6 weeks
Active spots per cell
Number of events
40
30
20
10
0
100
80
60
40
20
0
150
100
50
0
80
60
40
20
0
WT
KO
WT
KO
WT
KO
WT
KO

Figure S4

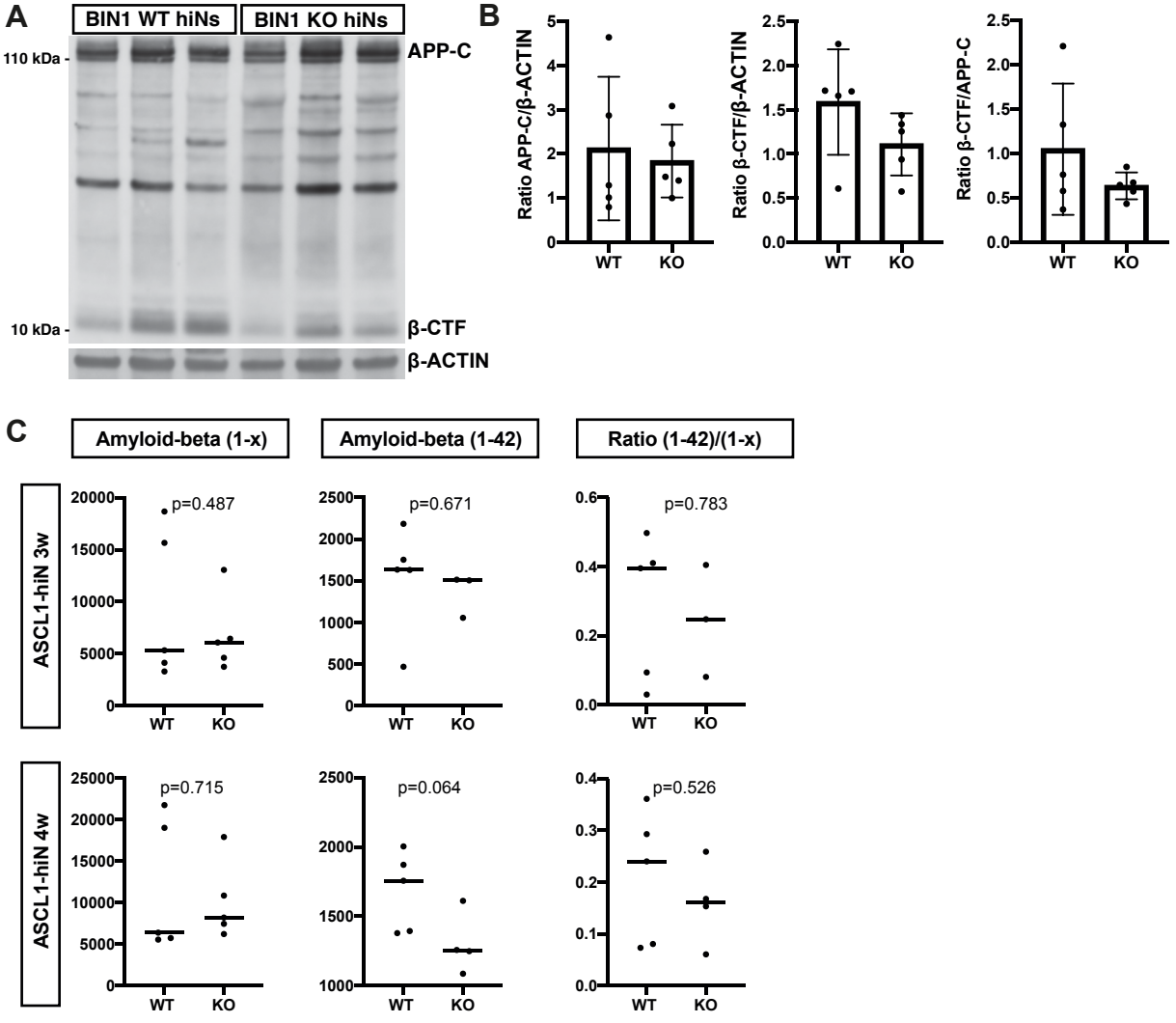
A
BIN1 WT hiNs
BIN1 KO hiNs
110 kDa -
APP-C
10 kDa -
β-CTF
β-ACTIN
B
Ratio APP-C/β-ACTIN
Ratio β-CTF/β-ACTIN
Ratio β-CTF/APP-C
WT
KO
C
Amyloid-beta (1-x)
Amyloid-beta (1-42)
Ratio (1-42)/(1-x)
ASCL1-hiN 3w
ASCL1-hiN 4w
p=0.487
p=0.671
p=0.783
p=0.715
p=0.064
p=0.526

Figure S5

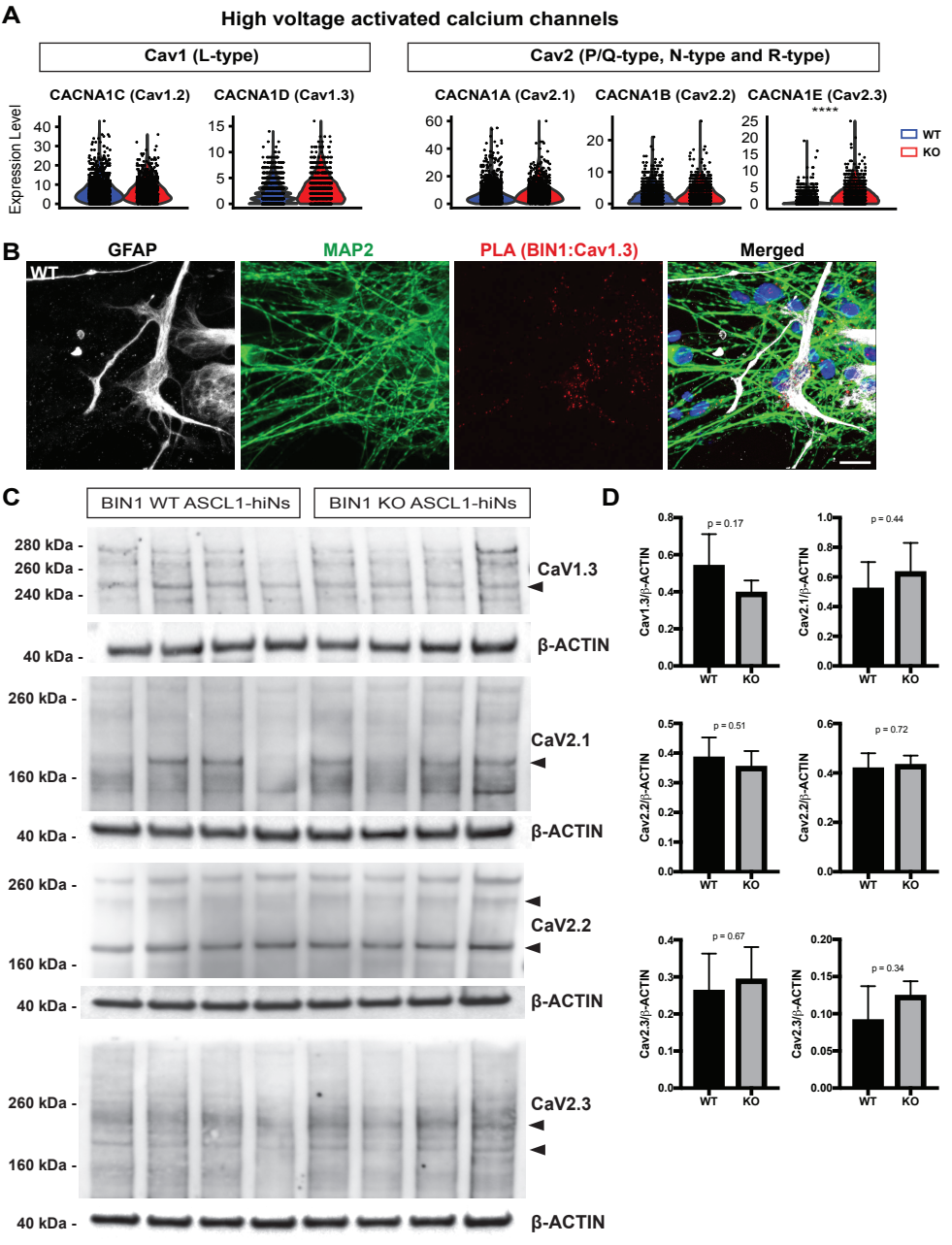
A
High voltage activated calcium channels
Cav1 (L-type)
Cav2 (P/Q-type, N-type and R-type)
CACNA1C (Cav1.2)
CACNA1D (Cav1.3)
CACNA1A (Cav2.1)
CACNA1B (Cav2.2)
CACNA1E (Cav2.3)
****
Expression Level
WT
KO
B
GFAP
MAP2
PLA (BIN1:Cav1.3)
Merged
WT
C
BIN1 WT ASCL1-hiNs
BIN1 KO ASCL1-hiNs
280 kDa -
260 kDa -
240 kDa -
CaV1.3
40 kDa -
β-ACTIN
260 kDa -
CaV2.1
160 kDa -
40 kDa -
β-ACTIN
260 kDa -
CaV2.2
160 kDa -
40 kDa -
β-ACTIN
260 kDa -
CaV2.3
160 kDa -
40 kDa -
β-ACTIN
D
Cav1.3/β-ACTIN
p = 0.17
Cav2.1/β-ACTIN
p = 0.44
Cav2.2/β-ACTIN
p = 0.51
Cav2.2/β-ACTIN
p = 0.72
Cav2.3/β-ACTIN
p = 0.67
Cav2.3/β-ACTIN
p = 0.34
WT
KO

Figure S6

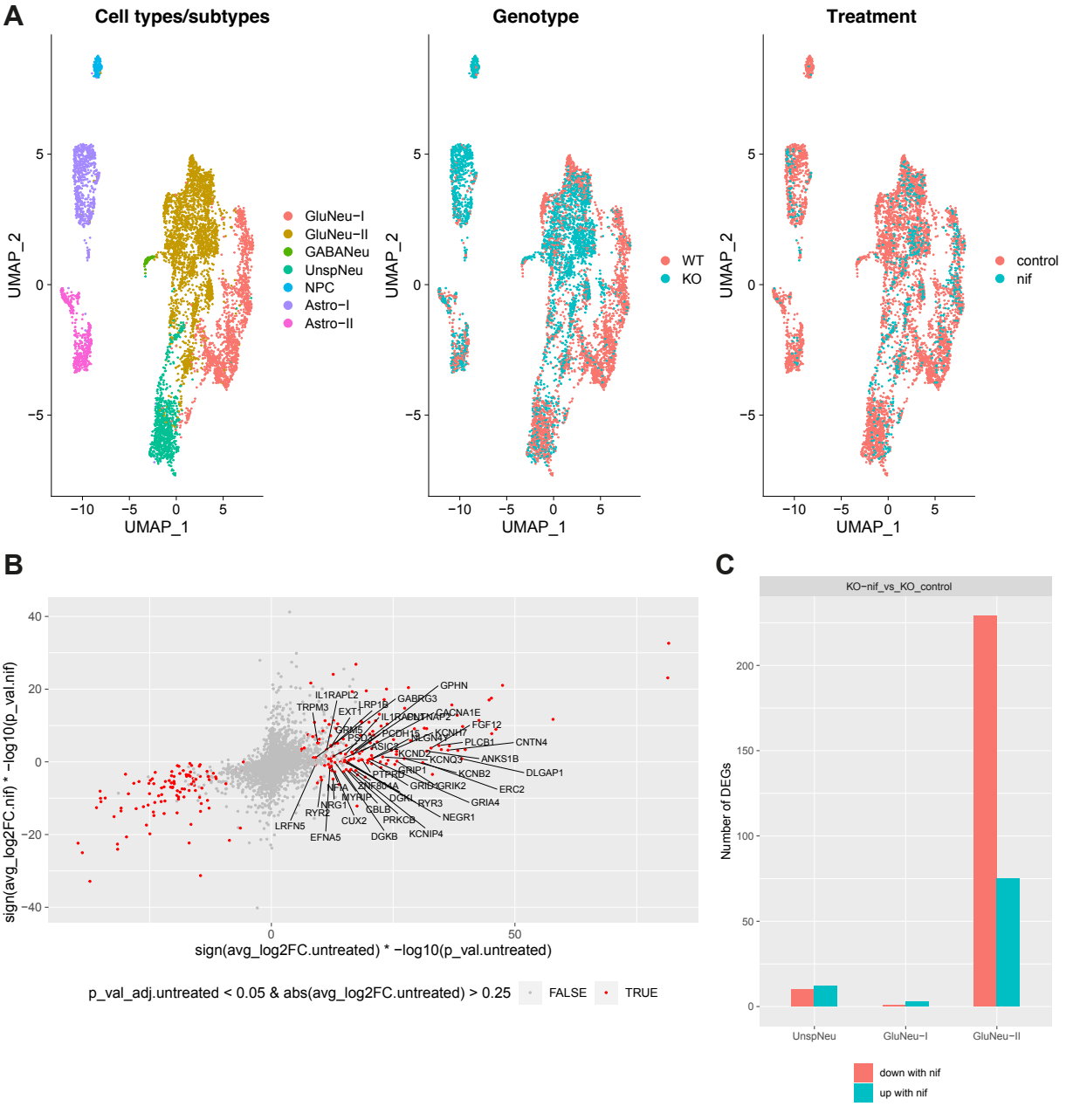
A
Cell types/subtypes
Genotype
Treatment
UMAP_1
UMAP_2
GluNeu−I
GluNeu−II
GABANeu
UnspNeu
NPC
Astro−I
Astro−II
WT
KO
control
nif
B
sign(avg_log2FC.nif) * −log10(p_val.nif)
sign(avg_log2FC.untreated) * −log10(p_val.untreated)
p_val_adj.untreated < 0.05 & abs(avg_log2FC.untreated) > 0.25
FALSE
TRUE
GPHN
GABRG3
CACNA1E
FGF12
CNTN4
PLCB1
ANKS1B
DLGAP1
KCNB2
ERC2
GRIA4
NEGR1
KCNIP4
DGKB
PRKCB
CUX2
CBLB
RYR3
DGKI
GRIK2
GRIP1
KCNQ3
KCND2
KCNH7
NLGN4
PCDH15
ASIC2
PSD4
GRM5
EXT1
LRP1B
IL1RAPL2
TRPM3
NFIA
MYRIP
NRG1
RYR2
LRFN5
EFNA5
C
KO−nif_vs_KO_control
Number of DEGs
UnspNeu
GluNeu−I
GluNeu−II
down with nif
up with nif